Li-ion cell safety monitoring using mechanical parameters, Part 1: normal battery operation

Angel Kirchev, Nicolas Guillet, David Brun-Buisson, Vincent Gau

Li-ion cell safety monitoring using mechanical parameters, Part 1: Normal battery operation

Journal:	*Journal of The Electrochemical Society*
Manuscript ID	JES-106284.R1
Manuscript Type:	Research Paper
Date Submitted by the Author:	n/a
Complete List of Authors:	Kirchev, Angel; CEA, LITEN guillet, Nicolas; CEA, LITEN Brun-Buisson, David; CEA, LITEN Gau, Vincent; CEA, LITEN
Keywords:	Batteries – Li-ion, 18650 cell, strain gauge, ultrasound interrogation, battery management

Li-ion cell safety monitoring using mechanical parameters, Part 1: Normal battery operation

A. Kirchev*, N. Guillet, D. Brun-Buission, V. Gau
Univ. Grenoble Alpes, CEA, Liten, Campus Ines, 50 Av. de Lac Leman, 73375 Le Bourget du Lac, France
Univ. Grenoble Alpes, CEA, Liten, 38000 Grenoble, France
*corresponding author e-mail: angel.kirchev@cea.fr

Key words: lithium ion battery, 18650 cell, strain gauge, ultrasound interrogation, battery management

Abstract

The normal operation of a 18650 Lithium-ion cells has been monitored using rectangular rosette strain gauge and a pair of piezoelectric transducers. The sensors for mechanical measurements provide information about the cell deformation mechanism and electrodes structure during the cycling. The strain gauge signal revealed three type of mechanical processes. The predominant deformation pattern during galvanostatic discharge process is an isotropic cylindrical shrinkage relevant to the extraction of lithium ions from the graphite negative electrode. In the case of low-rate discharge in cyclic voltammetry mode, the deformation pattern changes to spherical growth when the state of charge falls below 40. In contrast, the thermal shrinkage and growth of the cell corresponds to simple decrease of the cell diameter with much smaller hysteresis effect. The ultrasound interrogation is able to detect repeatable progressive change of the acoustic waveform transferred across the cell in direction of the jellyroll diameter, which depends on the state of charge and does not undergo any significant changes at different cycling rates. The impact of the state of health under 2h – rated charge/discharge cycling at 25°C reveals slow progressive drift of the strain and acoustic signals corresponding to the growth of the cell size.

The increase of the energy density of the Li-ion batteries is associated with the use of more reactive electrode materials, operating at extreme potentials. This leads to the appearance of safety issues when the cells approach or exceed the boundaries of their normal operating conditions. Such significant and severe safety issues are the thermal runaway and the subsequent battery fire processes. They can be triggered by a variety of external or internal mechanical, thermal and electric abuse events like cell crushing and piercing, overheating, short-circuiting or overcharge [1 - 3]. The prevention and the early detection of the thermal runaway are amongst the critical tasks of each Li-ion battery management and monitoring system (BMS). These tasks are carried out classically by the measurement of the cell voltage, current and battery proximity temperature and the subsequent data processing by the BMS software [4]. The battery parameters set can be further extended taking into account the mechanical behavior of the cells related to the phase changes in the electrode materials during the cycling and the ageing [5]. Two particular techniques amongst those discussed by Pop et al. in [5] are very attractive for practical use in medium and large scale Li-ion packs – the battery case deformation measurement and the acoustic ultrasound interrogation using piezoelectric transducers. Since the latter are rather inexpensive and compact, they have become an object of several recent experiential [6, 7] and theoretical [8] topic of interest.

The lithium-ion batteries undergo significant deformation during their regular operation due to the dynamics of the Li ions intercalation and extraction from the corresponding host materials. In the case of the so-called prismatic pouch-cell technology, the deformation practically coincides with the variation of the cell thickness. The corresponding relationship between the electrochemistry and the mechanics, which remains pretty much straight-forward, has been an object of intense experimental [9-13] and theoretical studies [14]. On the other hand, the pouch-cell technology allows assembly of battery packs using external compression in order to reduce the electrodes damage to the cyclic change of the thickness. The impact of this approach has been evaluated by the study of the evolution of the cell strains [15-17].

When the Li-ion cells employ cylindrical construction the evaluation of the electrodes geometric can be carried out by strain gauges attached on the cell surface [18-20] or integrated inside the jelly-roll stack [21]. In this case, the interpretation of the results becomes more complex due the confining impact of the cell casing on the jelly-roll expansion process during the discharge and *vice-versa*. Since the medium and large-scale battery pack manufacturing employing cylindrical cells has been demonstrated as successful technological and business strategy by Tesla Motors, it is interesting to study further and in more detail the mechanic behavior of this type of cells [22]. The focus of this work will be set on the normal battery operation, in order to get a background in the study of the kinetics of several abusive processes carried out in part two and part three of this series.

Experiment and methods

Lithium ion cells

The experiments have been carried out on commercially available cells from type INR18650 MJ1 manufactured by LG Chem (Republic of Korea). The nominal capacity of the cells is considered to be equal to 3400 mAh, and the rated values of the charge and discharge current are further referred versus this value. According to the product datasheet information, the cells can operate safely in the voltage range 2.5 ÷ 4.2 V using charge current limit equal to 3.4 A (1C, where C stands for the nominal capacity) and maximum discharge current of -10 A. The operating temperature rage in charge mode is from 0 to

45 °C, while the discharge can be carried out from -20 to +60 °C. The nominal energy density is equal to 252 $Wh.kg^{-1}$ and 748 $Wh.L^{-1}$. The charge/discharge experiments have been carried out using potentiostat-galvanostat BioLogic VSP (France). The experiments has been carried out in climate chamber or at room temperature. The cell skin temperature has been monitored during all experiments using K-type thermocouples attached with adhesive tape. The electrochemical tests have been comprised of constant current / constant voltage charge-discharge cycling with current varying from 3.4 A (1C) to 0.34 A (C/10h) as well as cyclic voltammetry with linear sweep rate of 50 $\mu V.s^{-1}$. The cell components has been characterized after the tear down analysis of completely discharged cell, using electronic microscopy coupled with EDX spectroscopy, thermal analysis (DSC), infrared spectroscopy (FTIR), X-ray diffraction, differential scanning calorimetry, and gas chromatography coupled with mass spectroscopy.

Stain gauge sensors and measurement equipment

The deformation of the cell casing is monitored by a general purpose rectangular rosette strain gauges type "C2A-06-062LR-120" manufactured by the company Micro-Measurements. The same company provided also the corresponding kit and instructions for metallic surface preparation and gauge bonding with cyanoacrylate glue, as well as a multi-channel measurement system. Detailed information about the gauge is presented in the supplementary information (S1). It is comprised of three encapsulated linear gauges reported on polyamide Kapton® substrate with a nominal resistance equal to 120 Ohm. The middle gauge (denoted as "J2") is orientated perpendicularly to the length of the sensor, while the other two sensors (denoted as "J1" and "J3") are inclined to 45° against the axe of the middle gauge (J1 stays on the side of the negative terminal). The gauge is made of constantan, a copper-nickel binary alloy that has a constant resistance over a large temperature range (*i.e.* the resistance changes due to the temperature variations can be related only to thermal expansion phenomena). The rosette is positioned in the middle of the cell length with measurement axis of gauge "2" perpendicular to the cell length, in order to detect the changes in the cell jelly-roll diameter with the best accuracy. During the cell deformation process the gauge pattern resistance increases proportionally to elongation according to the equation:

$$\frac{\Delta R}{R} = K\frac{\Delta L}{L} = K\varepsilon \qquad (1)$$

Where L and ΔL are the gauge pattern length and its variation, R and ΔR are the gage resistance and its resistance variation, K is the gauge factor and ε is the strain, which is expressed in $\mu m.m^{-1}$ or in ppm. The main advantage of the rosette gauge is related to the fact that it does not need to be positioned precisely with a perfect reproducibility taking into account all three signals together. Apart from the strains ε_1, ε_2, and ε_3, two deformation parameters *D* and *r* can be calculated as follows:

$$D = (\varepsilon_1 + \varepsilon_3)/2 \qquad (2)$$

$$r = \frac{1}{\sqrt{2}}\sqrt{(\varepsilon_1 - \varepsilon_2)^2 + (\varepsilon_2 - \varepsilon_3)^2} \qquad (3)$$

The graphic representation of the *r(D)* function allows rapid semi-quantitive interpretation of the deformation mechanism [23].

Acoustic ultrasound interrogation set-up

The acoustic measurements are carried out in ultrasound interrogation mode using a pair of lead

zirconate titanate ($Pb[Zr_xTi_{(1-x)}]O_3$ –PZT) ceramic, piezoelectric transducers, one operating as an emitter of ultrasound and the second as a receiver. In one first series of experiments, the acoustic coupling has been carried using high-end piezo-electric transducers R15-α (black / narrow bandwidth / emitter) and F15-α (white / wide bandwidth / receiver) manufactured by Euro Physical Acoustics. Same type of experiments have been repeated using low cost sensors from the type EPZ-20MS64W (6.4 kHz, 400 ohms), which possess similar footprint. The acoustic coupling set-up with both type of sensors attached on cells with strain gauges is presented in the supplementary information (S2). The acoustic signals were generated using WaveGen software (company Mistras) allowing defining the characteristics (frequency, duration, amplitude) of the electric signal by an electronic wave generator ARB-140. For the R15-α / F15-α transducers, signal emitted was a frequency sweeping between 100 and 200 kHz, 200 ms long, with a signal amplitude of 0.1 V. For the low cost EPZ-20MS64W transducers, the emitted signal had to be adapted to the and the frequency sweeping was only ranging between 120 and 150 kHz, while the duration was increased up to 1.5 ms and a signal amplitude of 1 V. The electric signal is converted in acoustic wave by the piezoelectric transducer operating in emission mode. The received acoustic signal is the transformed into voltage by the opposite piezoelectric transducer. The received signal is pre-amplified using a PCI2 module (company Mistras). The data acquisition is carried out using AEWin software and analyzed further using Noesis software and in-house developed machine-learning software [24]. The supplementary data (S3) presents the routine of the data analysis starting with the spectral transformation of the detected acoustic waveform and the subsequent clustering and mapping of the power spectra. The in-house developed machine-learning software allows pairing a given State of Charge (SOC) point to a corresponding power spectrum presented as a particular color in the 2D map.

Results and discussion

Lithium ion cell components

The inspection of the cell casing with SEM and EDX indicated that the iron and nickel are the main constituents of this component. The characterization of the separator material with DSC and FTIR showed that the material is composed of polyethylene. Its surface facing the negative electrode is coated with alumina. The separator thickness is about 8 µm. The results from the chromatographic analysis of the electrolyte indicated that the solvent is comprised of ethylene carbonate, dimethyl carbonate and propylene carbonate in approximate molar ratio of 6:3:1, being in good agreement with the literature [25]. The analysis of the positive electrode material with XRD, SEM and EDX showed that its principal constituent is $Li_xNi_{0.83}Mn_{0.07}Co_{0.1}O_2$ composition. It is fairly close to the commercial materials from the type NMC 811 having a specific capacity of about 200 $mAh.g^{-1}$ [26]. The measured surface loading is equal to 20.2 $mg.cm^{-2}$, resulting in an approximate specific capacity of 4.04 $mAh.cm^{-2}$. The same type of analysis applied on the negative electrode showed that it is comprised of graphite containing minor silicon content (detected as SiO_2). The surface loading of the negative electrode is 11.9 $mg.cm^{-2}$. The theoretical capacity of the negative active material is about 335 $mAh.g^{-1}$, considering a utilization of the graphite equal to 95 % (C_6 conversion to LiC_6) and the use of 5 % of conductive and binder additives. Thus, the specific capacity of the negative electrode should be about 3.99 $mAh.cm^{-2}$. This value is close enough to those of the positive electrode, allowing the assumption that both electrodes are “balanced” electrochemically.

Mechanic behavior of the cell during charge/discharge cycling

Figure 1 presents the evolution of the ensemble of battery parameters monitored during a short-term galvanostatic cycling with 2h-rated current at 25°C maintained in a climate chamber. During cycling, the cell skin temperature varies between 26 and 31°C, because the MJ1 technology corresponds to the so-called "energy" type and the applied current is close to the tolerance limits. The parameter SOC is calculated posteriori using amp-hour counting. Prior to this cycling, the cell has been completely recharged using constant current / constant voltage sequence (CC / CV, 1.7 A / 4.2 V) terminated when the current during the CV stage decreases to 0.17 A. After 30 min long rest period the strain signals measurement equipment has been reset. Thus, the reference point corresponding to zero deformation has been set to SOC = 100%. The data plotted in Figure 1c show that the strain evolution of all three gauges follows repeatable cyclic pattern that correlates well with the state of charge of the cell, being in good agreement with the literature [5, 18, 19].

The amplitude of the signal from the gauges J1 and J3 is roughly twice of the amplitude of the central gauge J2. This is an indication that the main type of cell deformation is due to the jellyroll diameter shrinkage during the discharge and expansion during the charge. It can be explained well with the fact that the graphite constituting the negative electrode material occupies largest volume fraction of the cell and it experiences most significant crystal lattice expansion due to the lithium ions intercalation (about 17%, [5]).

A closer inspection of the strain signal pattern shows that the relationship between the deformation and SOC is not perfectly straightforward. From one hand, there are small excursions of the strain in the initial and final stages of the discharge (*i.e.* the discharge starts and ends with short expansion periods). From the other, there is significant mechanical relaxation during the rest periods following the termination of the charge process. A hypothesis suggesting that the relaxation is linked with the temperature cool down could be rejected taking into account the fact that the heating is more intense in the end of the discharge where the amplitude of the relaxation is much smaller.

Figure 1d presents the evolution of the received acoustic signal strength during the constant current cycling measured by the couple piezo-electric transducers R15-α / F15-α. The selected parameter (the integrated voltage signal of entire waveform) allows a first order assessment of the mechanism of interaction of the cell with the probing ultrasound waves. It can be seen that the ultrasound interrogation results correlate with SOC in a way similar to the case of the strain evolution. This correlation suggests that the jellyroll shrinkage enhances some dampening effect or an increased absorption of the ultrasound waves and vice versa (the charging increases the jellyroll compacting which may enhance the passage of the ultrasound).

The results presented in Figure 2 illustrate the impact of the cycling current on the mechanic behavior of the cell. It can be seen that the evolution of the strain and the strength of the received acoustic signal follow similar pattern and amplitude, despite the increased cell temperature during the last cycle with 2 h rated current. The latter supports the above hypothesis that the impact of the Joule heat on the mechanic behavior of the cell during the 2 h – rated cycling is relatively small. The decrease of the cycling current leads to the appearance of much better pronounced regions (local minimums and maximums, changes of the slope) in the strain transients, which should correspond to the lithium ion insertion and extraction inside the different crystallographic phases, formed in the electrodes during the charge/discharge operation. The most significant impact of the current can be seen in the end of the charge process and the subsequent rest period. While the strain maximum reached at the moment of the current cut-off (4.2 V) remains rather constant, the subsequent relaxation process depends on the cycling

rate. It can be related to the fact that the lower charge current injects higher number of Amp-hours corresponding to slightly larger jellyroll diameter at steady state.

The strain data shown in Figure 2c have been subjected to the parametric analysis described (Equations 2 and 3). The corresponding results are plotted in Figure 3 together with a guiding diagram for qualitative interpretation of the deformation mechanism [23]. The data points corresponding to the rest periods between the charge and he discharge stages have been removed for the sake of simplicity. The results show that the deformation mechanism does not depend much on the applied cyclic rate, the only exception being the end of the charge domain. This finding is in fair agreement with the results of Ki-Yong Oh *et al.* [10], who reported relatively small change of the pouch cell swelling pattern going from 0.4C to 1C discharge.

The deformation pattern during most of the charge and discharge duration corresponds to a process combining cylindrical shrinkage and compression, *i.e.* isotropic growth of cylindrical body. The data corresponding to the charge and the discharge processes are clearly separated by an hysteresis loop which is related to the energy dissipation due to the lithium ion insertion and extraction from the host matrix of the positive and the negative electrode materials, as well as due to the changes of the separator porosity and the corresponding electrolyte displacement [14]. Since the strain values return rather close to their initial points in the end of each cycle the hysteresis can be considered as "elastic" type.

Figure 4a presents the results from the clustering and 2D mapping of the received ultrasound signal obtained during cycling with various charge rates and discharge rate fixed at C/2h at 25 °C. The measurements has been carried out with R15-α/F15-α couple of piezoelectric transducers. The different colors account for different types of waveforms defined from their power density spectra (same color = same DSP). Three waveform samples corresponding for different SOC values close to 0, 50 and 100 % are shown. The coupling of the acoustic and the electrochemical data is shown in Figure 4b and 4c using two type of x-axis in order to take into account the evolution of the data as a function of the time and SOC keeping the same color-code. It can be seen that nature of the transmitted acoustic signal changes with the change of the battery SOC almost independently on the applied charge rate. This result remains quite reproducible and it is consistent with the data presented in Figure 3c. The comparison of the data plotted in Figure 4 with those in Figure 2d shows that the acoustic interrogation is able to provide reliable and accurate data about the battery state without the necessity to development of precise physical mode representing the interaction of the cell jellyroll with the probing ultrasound.

Mechanic behavior of MJ1 Li-ion cell in cyclic voltammetry mode

The cyclic voltammetry with low voltage sweep rate (50 $\mu V.s^{-1}$) allows further assessment of the link between the kinetics of the charge/discharge reactions in the cell and its deformation. Figure 5 presents the evolution of the ensemble of battery parameters monitored during this type of test using another cell from the same purchase batch. The data are separated in two parts – the cathodic branch of the plots corresponds to the results measured during the voltage decrease from 4.2 to 2.5 V. Thus, the cathodic sweep can be considered as an alternative 10h rated discharge (its precise duration is equal to 9 h and 27 min). In the same way, the data recorded during the anodic voltage sweep from 2.5 to 4.2 V represent the kinetics of the charge reactions and the associated mechanic phenomena. The evolution of the three strain gauge signals is presented in Figure 5a. It can be seen that the amplitude of the deformation is lower in comparison with the previous case, however it remains in the same order of magnitude. In the voltage domain 3.5 – 4.2 V the signals of the gauges J1 and J3 are nearly identical and they are twice lower than those of J2. These data indicated that the discharge process in this voltage domain

corresponds to a cell shrinkage with relatively homogeneous spatial distribution of the local current density. This means than at high SOC values most of the deformation can be related to the lithium ion insertion and extraction from the graphite negative electrode. When the voltage is lower than 3.5 V, the discharge process continues with partial recovery of the cell volume (swelling), which can be linked with the lithium ion insertion in the host matrix of the positive NMC electrode. Here the difference between the signals of the gauges J1 and J3 indicates certain non-homogeneity of the current density distribution. Such type of artefact can be possibly related to the radial positioning of the strain gauge rosette, which cannot be predicted or controlled without preliminary X-ray tomography (e.g. rosette installed in close proximity to the jellyroll foil edge or coating ending).

The parametric analysis of the strain pattern presented in Figure 5b remains similar to those shown in Figure 3. The data corresponding to the anodic and the cathodic sweep are separated by a hysteresis of nearly 60 ppm in direction of both axis, which is fairly close to the hysteresis observed in Figure 3 (about 50 ppm in both directions). The *r(D)* curve contains 4 kink points indicating drastic changes of the mechanism of the cell deformation. The origin of the points corresponding to cell voltage equal to 2.5 and 4.2 V is clear – it corresponds to the termination of the processes of discharge and charge. Both remaining points correspond to cell voltage values close to 3.5 V, *i.e.* they are located in the region of the transition from shrinkage to expansion and *vice versa*. The slope of the parametric function *r(D)* in both regions is distinctly different indicating different mechanisms of expansion and shrinkage of the positive and the negative electrode. It was already mentioned that at higher SOC values, the negative electrode contributes more to the cell deformation and the latter undergoes isotropic cylindrical expansion and shrinkage.

In contrast, it can be seen that the deep discharge carried out in voltammetry mode reveals that the positive electrode contributes to deformation with spherical pattern.

Both sweeps of the classic voltammogram has been separated in order to compare the current with the strain rate (the time derivative of the strain). Since the strain rate of all three gauges follows identic pattern only the parameter corresponding to the gauge J2 is presented in Figure 5c and 5d. The comparison of the strain rate with the current is very convenient because both parameters are time derivatives of physical terms related to the size of the electrochemical cell (diameter, length and charge storage capacity). The sign of the strain rate indicates the deformation type (shrinkage or expansion), while the appearance of minimums and maximums indicates the occurrence of electrochemical reactions. It can be seen that there is a fair correspondence between the number and the position of the current peaks of the strain rate minimums and maximums, which is in good agreement with the theoretical considerations of Schiffer *et al.* [27].

Impact of the temperature on the mechanic behavior of MJ1 Li-ion cells

The impact of the temperature on the mechanic behavior of the MJ1 cells has been evaluated in two different types of experiments. During the first one, completely charged cell equipped with strain gauge rosette has been subjected to a short thermal cycling between -5 and +45 °C using the stair-case like profile shown in Figure 6a. The same plot presents also the evolution of the signals from the three strain gauges. It can be seen that the mechanical response to the change of the temperature is very rapid. It also includes strain relaxation effects with an amplitude increasing over the temperature. The strain *vs.* temperature plots presented in Figure 6b show that the thermal dependence of the deformation is not linear and it features a hysteresis effect which is more pronounced at the higher temperatures. The distinct difference between the inclined gauges J1 and J3 and the central gauge remains, which indicates

that considerable part of the thermal effect on the strain signal is related to the mechanical changes of the cell. If we consider that the thermal dependence of the gauge factors remain close to linear, the parametric analysis of the r(D) function can be applied in order to analyses the deformation mechanism related to the changes of the temperature. The corresponding result presented in Figure 6c differs significantly from the data discussed in the previous paragraphs. It can be seen that temperature changes can be associated with nearly ideal shrinkage and expansion of the cell diameter. The hysteresis effects are also much smaller, which indicates that the hysteresis observed in Figure 3 and 5b are caused by the energy dissipation corresponding to the occurrence of the electrochemical reactions.

Figure 7 presents the results from the clustering and 2D mapping of the received ultrasound signal obtained during cycling with 2h-rated charge and discharge current at three different temperatures (5, 25 and 45 °C). Again, the study has been carried out with R15-α/F15-α couple of sensors. As expected, the increase of the temperature increases the capacity and the energy efficiency of battery, the latter being directly evident as decreased voltage hysteresis. It can be seen that the temperature impacts also strongly the waveform of the received ultrasound signal at a fixed cell voltage (respectively fixed SOC value) indicating that the thermal expansion of the cell influences its interaction with the ultrasound. The increase of SOC increases the difference between the acoustic waveform patterns. A smaller variation of the waveform pattern at very low SOC can be seen in Figure 7d. These results can be further related to the fact that the cell jellyroll is the most compact when SOC is close to 0 %, and the additional shrinkage caused by the cooling will not alter substantially the transfer of the ultrasound waves across the cell.

Impact of the cycling aging on the mechanic behavior of MJ1 Li-ion cells

A MJ1 Li-ion cell equipped with strain gauge rectangular rosette and a pair of low cost piezoelectric transducers from the type EPZ-20MS64W has been subjected to charge/discharge cycling with 2h-rated current and depth of discharge equal to 100 % (DOD = 100 %) at room temperature (22 °C +/- 1 °C). Figure 8a and 8b present the impact of the ageing on the classic battery parameter set (current, voltage, temperature and capacity). As expected, the capacity decreases and the internal resistance increases progressively without any significant change of the cell skin temperature. The strain data presented in Figure 8c-8e show that the cycle ageing takes place without causing any significant change of the overall deformation pattern. The most visible impact of the ageing is an increasing amplitude of the signal corresponding to increased cell swelling in charge mode followed by relaxation. In contrast, the strain measurements at open circuit in completely charged state increase with much slower rate especially until 400 cycles. This result indicates that the stress effects associated with the increased swelling of the cell (corresponding on its turn to the lithium ions intercalation in the graphite) are dynamic. This mechanic phenomenon is quite similar to the increased charge voltage due to the higher internal resistance of the cell. According to the works of Cannarella and Arnold [28] and Jones et al. [29] the Li-ion cell swelling due the cyclic deterioration can be related mostly to the processes associated with the growth of the passivation layer (so-called “solid electrolyte interface”) between the graphite particles and the non-aqueous electrolyte.

The parametric analysis of the strain data presented in Figure 8f shows that the predominant deformation pattern remains the isotropic growth and shrinkage of a cylindrical body. However the shift of the curves in right-hand direction indicates that the cell swelling caused by the cycling ageing follows a pattern corresponding to a spherical growth, which has been identified as an effect caused by the operation of the positive electrode. Another minor consequence from the ageing is a small decrease of the hysteresis

of the *r(D)* plots. This effect can be explained supposing that that the hysteresis corresponds to a certain energy storage capacity. Thus, the large hysteresis corresponding to the charge/discharge cycling can be related to the large electric energy storage capacity (12.6 Wh) and the much small hysteresis observed during the thermal cycling will be due to the much smaller heat storage capacity (0.68 Wh considering C_p = 1 $J.g^{-1}K^{-1}$ and ΔT = 50 K [30]). Using the same consideration we can link the decreasing capacity with the decreasing hysteresis of the *r(D)* plots.

The results from the ultrasound interrogation at different state of health using an acoustic set-up with low cost piezoelectric transducers are plotted in Figure 8g. It can be seen that in this narrow frequency range of acoustic interrogation (120 – 150 kHz), the signal strength dependence on SOC follows an inversed trend – it decreases during the charge and vice versa. The range of this parameter is about one order of magnitude higher. This kind of differences can be explained by the different characteristics of the low cost transducers (e.g. frequency bandwidth, input impedance, coupling mechanism, etc….). No matter of this, the measurements remain rather stable. The effect of the aging is mostly visible at the plateau regions corresponding to the open circuit periods. In this case, the decrease of the capacity correlates with decrease of the signal strength. Figure 8h indicates that the correlation is close to linear, especially when the cell is completely discharged. This result is in good agreement with the work of Gaul et al, which studied bigger pouch-cell Li-ion batteries with similar methodology [7].

The continuous monitoring of both types of mechanical parameters during long-term cycling shows that the impact of the state of charge remains predominant, while those of the state of health cause a slow, rather monotonic drift of the observed mechanical characterization signals.

The stability of the observed signals indicates that the approach can be used further in practical applications after minor changes of the sensors wiring and position. In the case of the strain gauges, it can be a transition from soldered wires towards sliding pins, which can contact the corresponding pins installed on the walls of the battery modules. The paired piezoelectric transducers themselves can be integrated inside the void spaces which are formed naturally between the cylindrical cells in the module. In it expected that such integration will be even easier at the forthcoming cell format 4280 [22].

Conclusions

Two different types of non-invasive mechanical characterization methods have been used simultaneously for extended battery monitoring during its normal operation. Both type of parameters correlate well with the state of charge and the temperature in a stable and repetitive way. The use of rectangular strain gauge rosette and parametric analysis of the signals allows distinguishing two different deformation mechanisms corresponding to the expansion and shrinkage of each electrode due to the intercalation and extraction of the lithium ions. Both electrode shrinkage/expansion mechanisms differs from the deformation caused by the change of the temperature. The acoustic interrogation data show strong dependence on the state of charge and the temperature, especially when the results are analyzed with data-mining tools based on signal clustering and mapping of the power density spectra. It has been found that the method can be also applied successfully using low cost piezoelectric transducers, which provide accurate and stable data during long term cycling aging tests. The acoustic data during such tests undergo rather slow evolution indicating the robustness of the acoustic interrogation as a method for monitoring of the normal battery operation.

Acknowledgement

This work has been realized in association with INES.2S within the French national program Investments for the Future (ANR-10-IEED-0014-01) and received funding from the European Union's Horizon 2020 research and innovation program under the grant 'Electric Vehicle Enhanced Range, Lifetime And Safety Through INGenious battery management' (Project EVERLASTING-713771).

References

1. T.M. Bandhauer, S. Garimella, and T.F. Fuller, J. Electrochem. Soc., **158**, R1 (2011)
2. H. Liu, Z. Wei, W. He, J. Zhao, Energy Conversion and Management, **150**, 304 (2017)
3. X. Feng, M. Ouyang, X. Liu, L. Lu, Y. Xia, X. He, Energy Storage Materials, **10**, 246 (2018)
4. J. Warner, "The Handbook of Lithium-Ion Battery Pack Design", Elsevier, Amsterdam, 2015, p. 91
5. H. Popp, M. Koller, M. Jahn, A. Bergmann, J. Energy Storage **32**, 101859, (2020)
N6. L. Gold, T. Bach, W. Virsik, A. Schmitt, J. Müller, T.E.M. Staab, G. Sextl, J. Power sources **343**, 536 (2017)
7. T. Gaul, U. Lieske, K. Nikolowski, P. Marcinkowski, M. Wolter, L. Schubert, (2021) "Monitoring of Lithium-Ion Cells with Elastic Guided Waves", in Rizzo P., Milazzo A. (eds) European Workshop on Structural Health Monitoring (EWSHM 2020), Lecture Notes in Civil Engineering, vol 128, Springer, Cham. https://doi.org/10.1007/978-3-030-64908-1_69
8. Gao Jie, Lyu Yan, Zheng Mingfang, Liu Mingkun, Liu Hongye, Wu Bin, He Cunfu, Appl. Acoustics **184**, 108356 (2021)
9. M. Hahn, H. Buqa, P.W. Ruch, D. Goers, M.E. Spahr, J. Ufheil, P. Novák, and R. Kötz, Electrochem. Solid State Lett., **11**, A151 (2008)
10. Ki-Yong Oh, Jason B. Siegel, Lynn Secondo, Sun Ung Kim, Nassim A. Samad, Jiawei Qin, Dyche Anderson, Krishna Garikipati, Aaron Knobloch, Bogdan I. Epureanu, Charles W. Monroe, Anna Stefanopoulou, J. Power Sources **267**, 197 (2014)
11. P.K. Leung, C. Moreno, I. Masters, S. Hazra, B. Conde, M.R. Mohamed, R.J. Dashwood, R. Bhagat, J. Power Sources **271**, 82 (2014)
12. B. Rieger, S. Schlueter, S.V. Erhard, J. Schmalz, G. Reinhart, A. Jossen, J. Energy Storage, **6**, 213 (2016)
13. M. Bauer, M. Wachtler, H. Stöwe, J.V. Persson, M.A. Danzer, J. Power Sources **317**, 93 (2016)
14. D. Sauerteig, N. Hanselmann, A. Arzberger, H. Reinshagen, S. Ivanov, A. Bund, J. Power Sources **378**, 235 (2018)
15. Ximing Cheng and Michael Pecht, Energies **10**, 591 (2017)
16. Ph. Daubinger, F. Ebert, S. Hartmann, G.A. Giffin, J. Power Sources **488**, 229457 (2021)
17. T. Deich, M. Storch, K. Steiner, A. Bund, J. Power Sources **506**, 230163 (2021)
18. Liyuan Feng, Shuo Zhou, Yancheng Li, Yao Wang, Qiang Zhao, Chunhui Luo, Guixin Wang, Kangping Yan, J. Energy Storage, **16**, 84 (2018)

19. L. Willenberg, P. Dechent, G. Fuchs, M. Teuber, M. Eckert, M. Graff, N. Kürten, .D.U. Sauer, E. Figgemeier, J. Electrochem. Soc., **167**, 120502 (2020)

20. L.K. Willenberg, Ph. Dechent, G. Fuchs, D.U. Sauer and E. Figgemeier, Sustainability **12**, 557 (2020)

21. Shengxin Zhu, Le Yang, Jiawei Wen, Xiaolong Feng, Peijun Zhou, Fuguo Xie, Jiang Zhou, Ya-Na Wang, J. Power Sources **516**, 230669 (2021)

22. Fred Lambert, electrec website, Feb. 3rd 2021, available online at https://electrek.co/2021/02/03/panasonic-plans-tesla-4680-battery-cell-production/

23. Jean Avril, "Encyclopédie Vishay d'analyse des contraintes encyclopédie", NT 58C "Interpretation des mesures extensometriques", Micromesures, 1984

24. L. Oca, N. Guillet, R. Tessard, U. Iraola, J. Energy Storage, **23**, 29 (2019)

25. J. Sturm, A. Rheinfeld, I. Zilberman, F.B. Spingler, S. Kosch, F. Frieb, A. Jossen, J. Power Sources, **412**, 204 (2019)

26. NEI Corporation, "Lithium Nickel Manganese Cobalt Oxide (NMC811) electrode sheets", product brochure available online at https://www.neicorporation.com/specs/NANOMYTE_BE-56E_NMC811_Spec_Sheet.pdf

27. Z.J. Shiffer, J. Cannarella, and C.B. Arnold, J. Electrochem. Soc. **163**, A427 (2016)

28. J. Cannarella, and C.B. Arnold, J. Power Sources **269**, 7 (2014)

29. E.M.C. Jones, Ö.Ö. Çapraz, S.R. White, and N.R. Sottos, J. Electrochem. Soc. **163**, A1965 (2016)

30. H. Maleki, S. Al Hallaj, J.R Selman, R.B. Dinwiddie, H. Wang, J. Electrochem. Soc., **146**, 947 (1999)

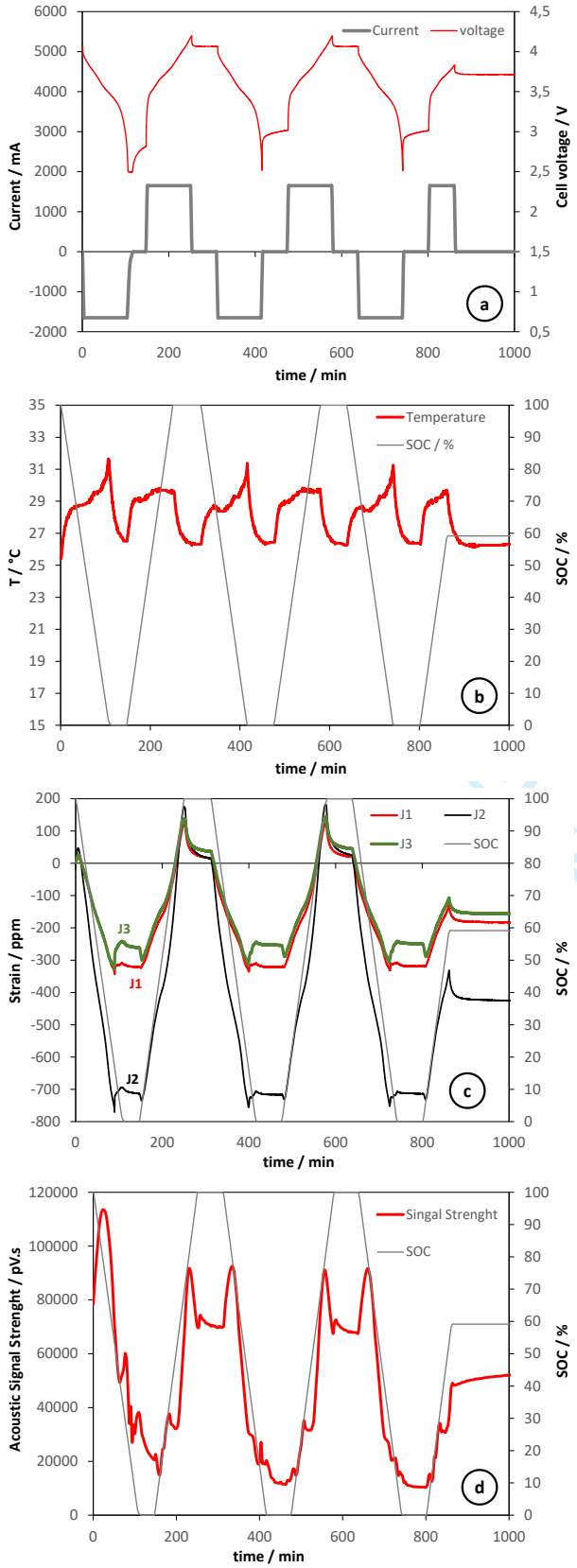

Fig. 1. Evolution of the battery parameters during galvanostatic cycling with C/2h rated current.

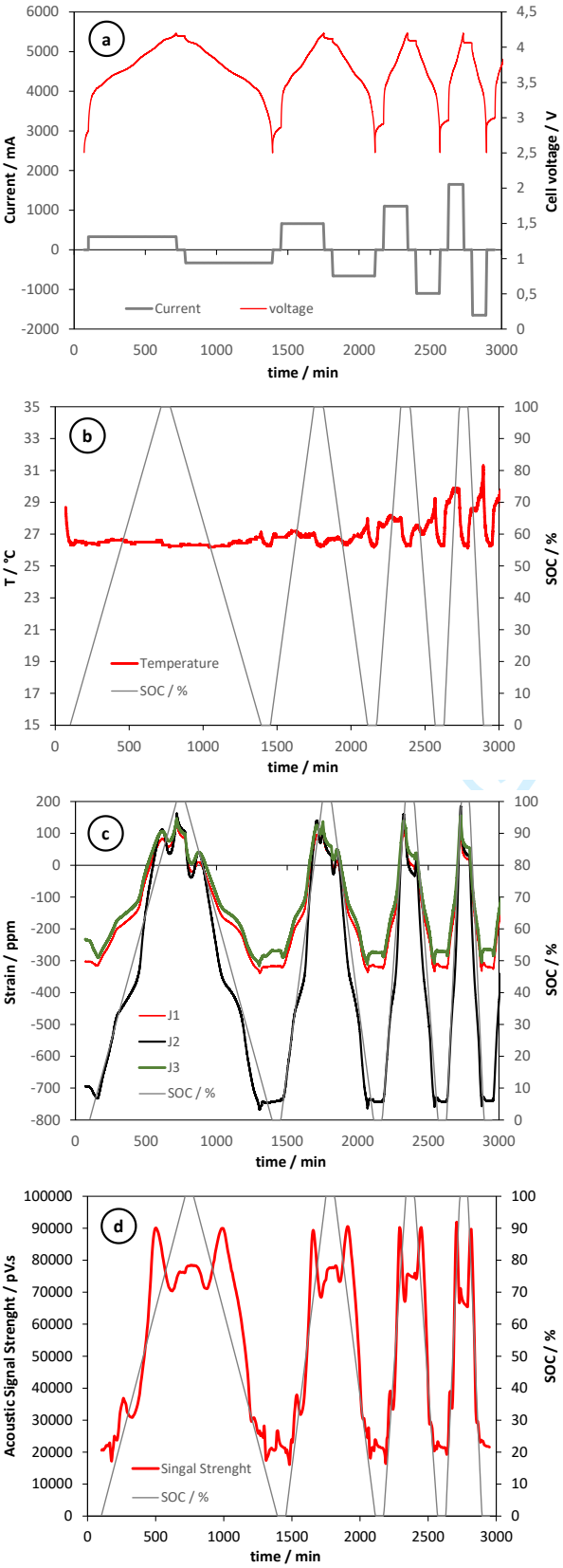

Fig. 2. Evolution of the battery parameters during galvanostatic cycling with current equal to C/10h, C/5h, C/3h and C/2h.

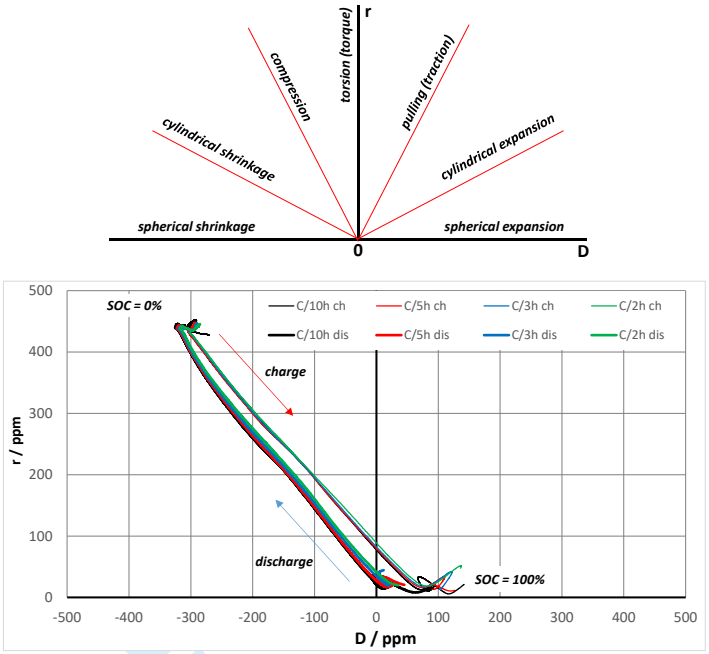

Fig. 3. Parametric analysis diagram for qualitative interpretation of strain measurements carried out by rectangular rosette gage and experimental r(D) patterns obtained during cycling of MJ1 cell with different currents at 25 °C

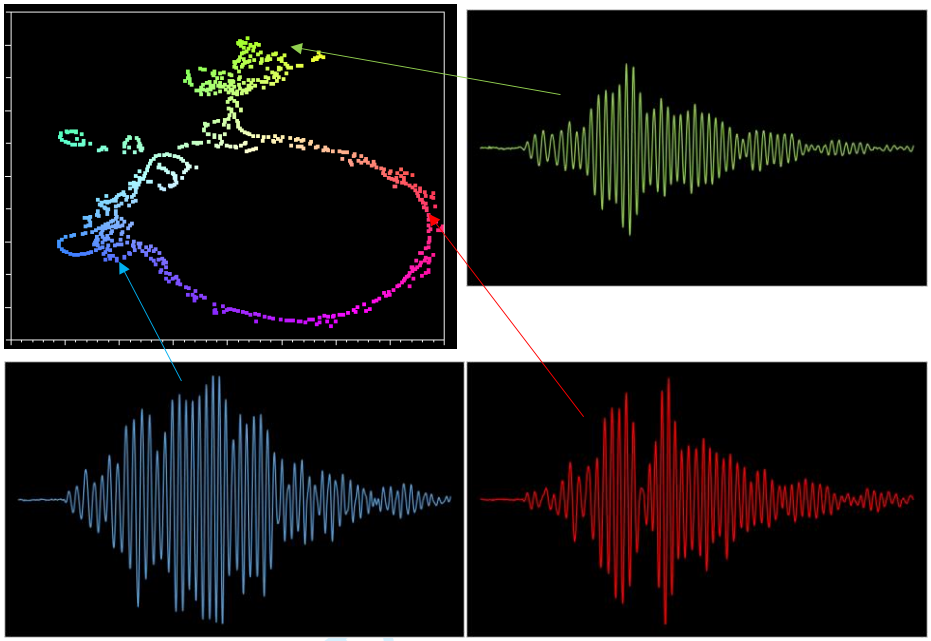

(a)

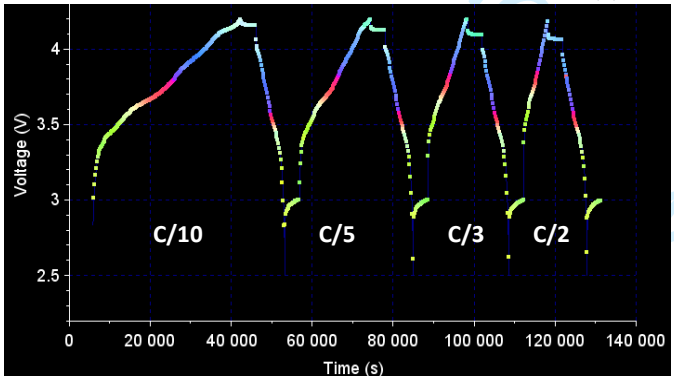

(b)

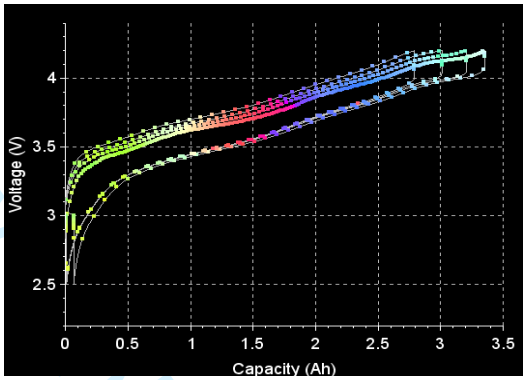

(c)

Fig. 4. Results from the ultrasound interrogation of Li-ion cell INR 18650 MJ1 during cycling with various charge rates and discharge rate fixed at $C_n/2h$ at 25°C (a, b) using clustering and 2D mapping of the acoustic data (c).

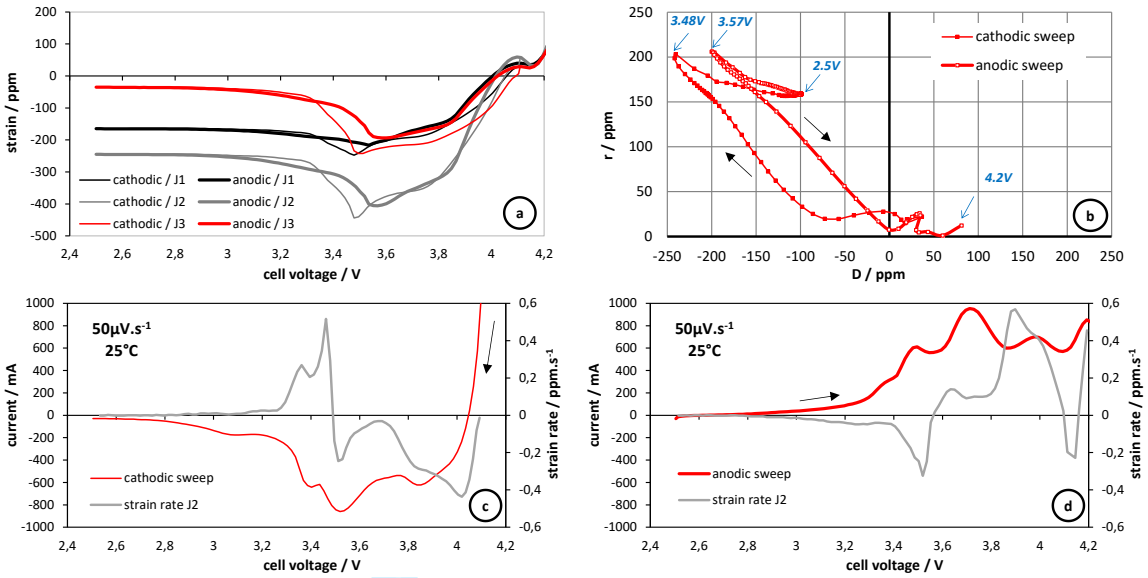

Fig. 5. Evolution of the cell strain (a), current and strain rate (c and d) during voltammetry cycle with sweep rate equal to 50µV.s^{-1} at 25°C, together with the corresponding parametric analysis of the deformation data (b).

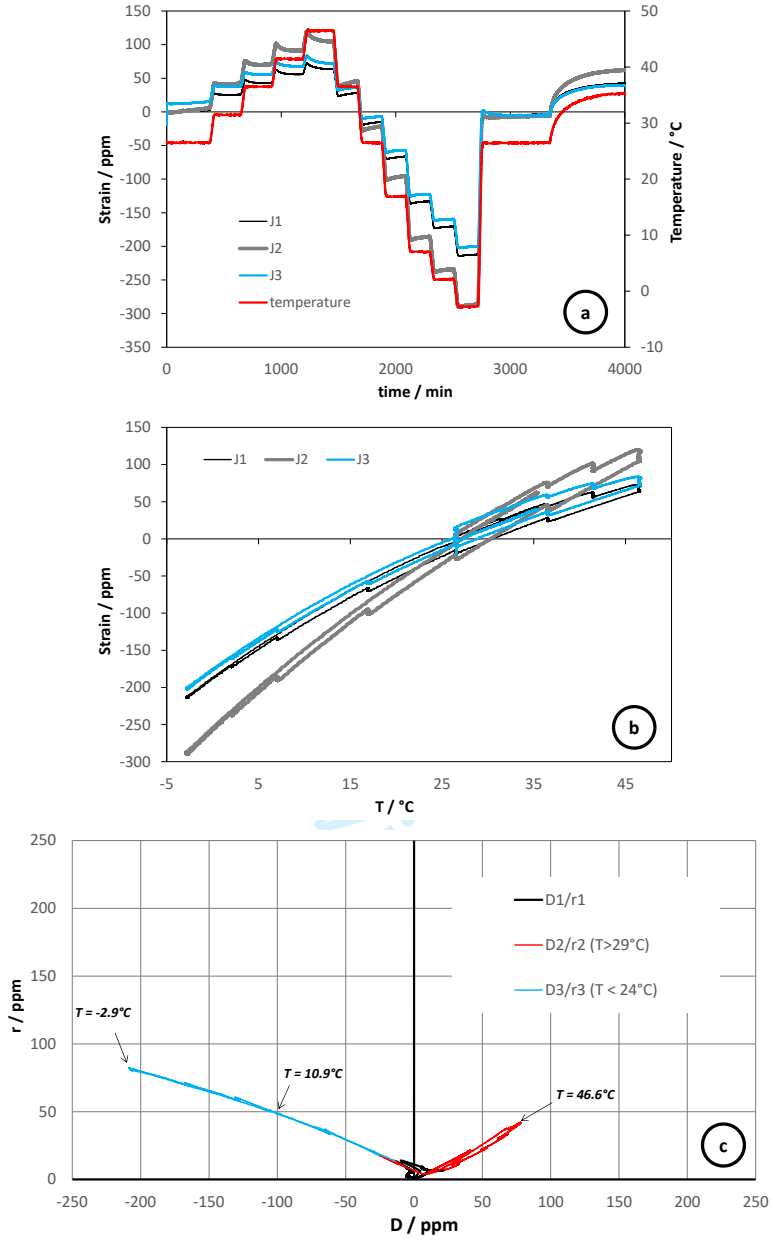

Fig. 6. Impact of the temperature on the strain signal at SOC = 100% (a and b) and parametric analysis of the strain data during the thermal cycling (c). The domains D1/r1, D2/r2 and D3/r3 indicate data points measured corresponding to three different temperature ranges.

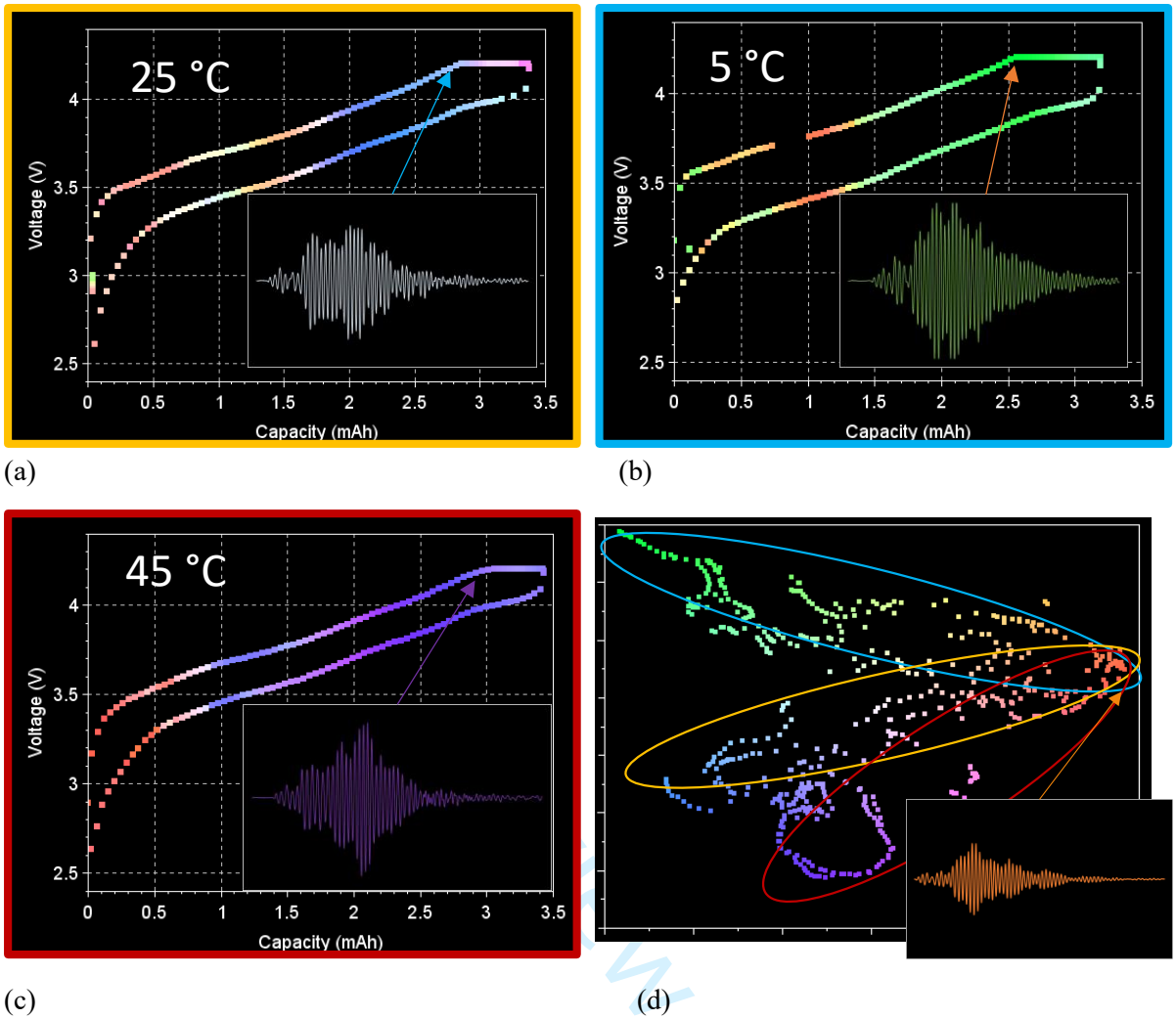

Fig. 7. Results from the ultrasound interrogation of Li-ion cell INR 18650 MJ1 during cycling at three different temperatures with 2h-rated charge and discharge current (a, b and c). Clustering and 2D mapping of the results measured at the different temperatures (d).

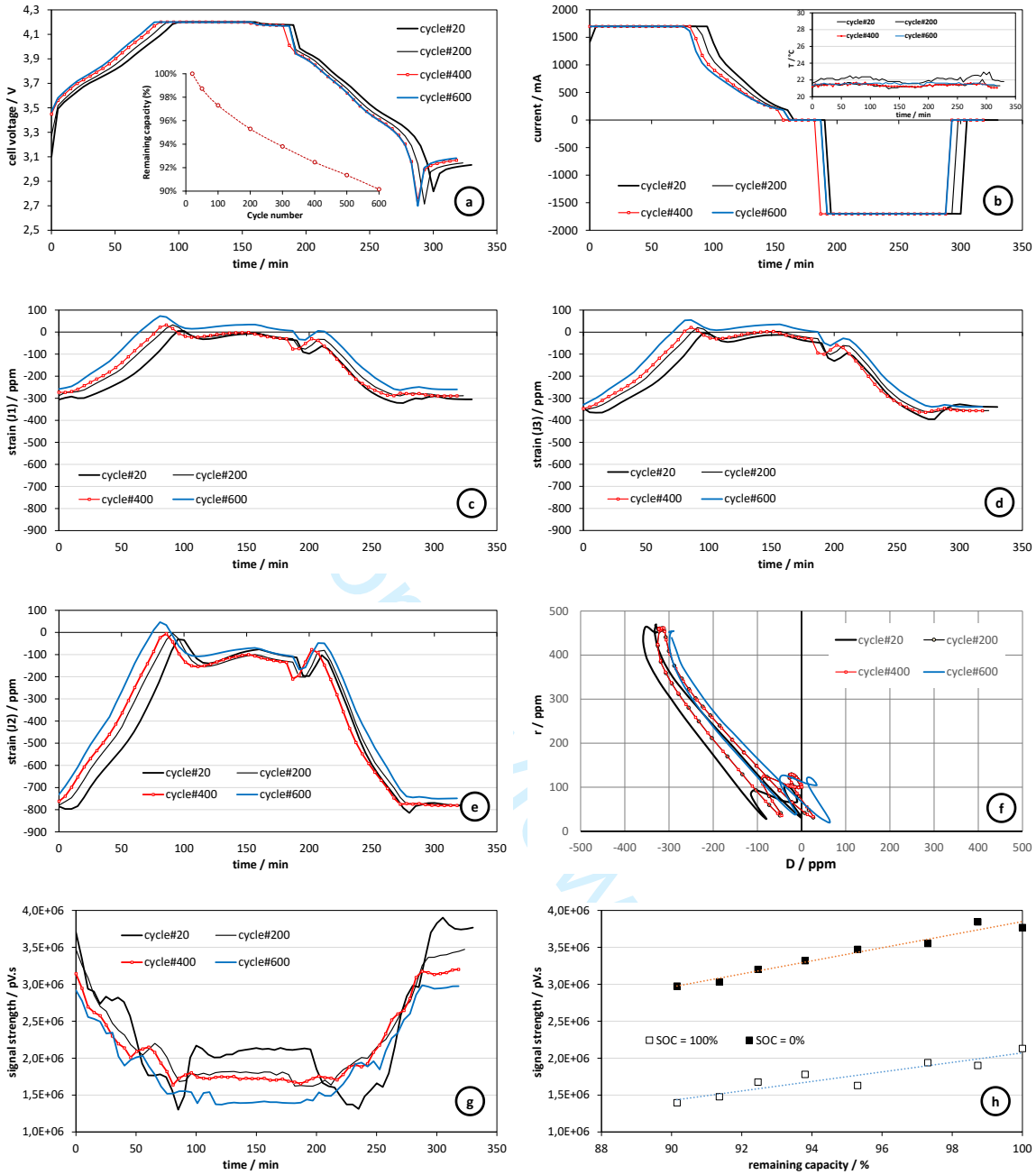

Fig. 8. Impact of the cycling ageing on the electrochemical and mechanical behavior of Li-ion cell INR 18650 MJ1.

Li-ion cell safety monitoring using mechanical parameters, Part 1: Normal battery operation

A. Kirchev*, N. Guillet, D. Brun-Buission, V. Gau
Univ. Grenoble Alpes, CEA, Liten, Campus Ines, 50 Av. de Lac Leman, 73375 Le Bourget du Lac, France
Univ. Grenoble Alpes, CEA, Liten, 38000 Grenoble, France
*corresponding author e-mail: angel.kirchev@cea.fr

Key words: lithium ion battery, 18650 cell, strain gauge, ultrasound interrogation, battery management

Abstract

The normal operation of a 18650 Lithium-ion cells has been monitored using rectangular rosette strain gauge and a pair of piezoelectric transducers. The sensors for mechanical measurements provide information about the cell deformation mechanism and electrodes structure during the cycling. The strain gauge signal revealed three type of mechanical processes. The predominant deformation pattern during galvanostatic discharge process is an isotropic cylindrical shrinkage relevant to the extraction of lithium ions from the graphite negative electrode. In the case of low-rate discharge in cyclic voltammetry mode, the deformation pattern changes to spherical growth when the state of charge falls below 40. In contrast, the thermal shrinkage and growth of the cell corresponds to simple decrease of the cell diameter with much smaller hysteresis effect. The ultrasound interrogation is able to detect repeatable progressive change of the acoustic waveform transferred across the cell in direction of the jellyroll diameter, which depends on the state of charge and does not undergo any significant changes at different cycling rates. The impact of the state of health under 2h – rated charge/discharge cycling at 25°C reveals slow progressive drift of the strain and acoustic signals corresponding to the growth of the cell size.

The increase of the energy density of the Li-ion batteries is associated with the use of more reactive electrode materials, operating at extreme potentials. This leads to the appearance of safety issues when the cells approach or exceed the boundaries of their normal operating conditions. Such significant and severe safety issues are the thermal runaway and the subsequent battery fire processes. They can be triggered by a variety of external or internal mechanical, thermal and electric abuse events like cell crushing and piercing, overheating, short-circuiting or overcharge [1 - 3]. The prevention and the early detection of the thermal runaway are amongst the critical tasks of each Li-ion battery management and monitoring system (BMS). These tasks are carried out classically by the measurement of the cell voltage, current and battery proximity temperature and the subsequent data processing by the BMS software [4]. The battery parameters set can be further extended taking into account the mechanical behavior of the cells related to the phase changes in the electrode materials during the cycling and the ageing [5]. Two particular techniques amongst those discussed by Pop et al. in [5] are very attractive for practical use in medium and large scale Li-ion packs – the battery case deformation measurement using strain gauges and the acoustic ultrasound interrogation using piezoelectric transducers. Both methods use rather inexpensive and compact sensors and transducers and do not require too sophisticated electronics for data acquisition and treatment. These advantages are the main reason for this study, which will focus first on the investigation of the mechanical behavior of cylindrical Li-ion cells under normal operation. The success of the Tesla Motors electric vehicles and the recently announced intention to keep the cylindrical cell construction with opposite terminals in their future energy storage products brought additional motivation to do this study using cylindrical cells [6].

Experiment and methods

Lithium ion cells

The experiments have been carried out on commercially available cells from type INR18650 MJ1 manufactured by LG Chem (Republic of Korea). The nominal capacity of the cells is considered to be equal to 3400 mAh, and the rated values of the charge and discharge current are further referred versus this value. According to the product datasheet information, the cells can operate safely in the voltage range 2.5 ÷ 4.2 V using charge current limit equal to 3.4 A (1C) and maximum discharge current of -10 A. The operating temperature rage in charge mode is from 0 to 45 °C, while the discharge can be carried out from -20 to +60 °C. The nominal energy density is equal to 252 $Wh.kg^{-1}$ and 748 $Wh.L^{-1}$. The charge/discharge experiments have been carried out using potentiostat-galvanostat BioLogic VSP (France). The experiments has been carried out in climate chamber or at room temperature. The cell skin temperature has been monitored during all experiments using K-type thermocouples attached with adhesive tape.

The cell components has been characterized after the tear down analysis of completely discharged cell, using electronic microscopy coupled with EDX spectroscopy, thermal analysis (DSC), infrared spectroscopy (FTIR), X-ray diffraction, differential scanning calorimetry, and gas chromatography coupled with mass spectroscopy.

Stain gauge sensors and measurement equipment

The deformation of the cell casing is monitored by a general purpose rectangular rosette strain gauges type “C2A-06-062LR-120” manufactured by the company Micro-Measurements. The same company provided also the corresponding kit and instructions for metallic surface preparation and gauge bonding with cyanoacrylate glue, as well as a multi-channel measurement system. Detailed information about the gauge is presented in the supplementary information (S1). It is comprised of three encapsulated linear gauges

reported on polyamide Kapton® substrate with a nominal resistance equal to 120 Ohm. The middle gauge (denoted as "J2") is orientated perpendicularly to the length of the sensor, while the other two sensors (denoted as "J1" and "J3") are inclined to 45° against the axe of the middle gauge (J1 stays on the side of the negative terminal). The gauge is made of constantan, a copper-nickel binary alloy that has a constant resistance over a large temperature range (*i.e.* the resistance changes due to the temperature variations can be related only to thermal expansion phenomena). The rosette is positioned in the middle of the cell length with measurement axis of gauge "2" perpendicular to the cell length. During the cell deformation process the gauge pattern resistance increases proportionally to elongation according to the equation:

$$\frac{\Delta R}{R} = K\frac{\Delta L}{L} = K\varepsilon \qquad (1)$$

Where L and ΔL are the gauge pattern length and its variation, R and ΔR are the gage resistance and its resistance variation, K is the gauge factor and ε is the strain, which is expressed in $\mu m.m^{-1}$ or in ppm. The main advantage of the rosette gauge is related to the fact that it does not need to be positioned precisely with a perfect reproducibility taking into account all three signals together. Apart from the strains ε_1, ε_2, and ε_3, two deformation parameters D and r can be calculated as follows:

$$D = (\varepsilon_1 + \varepsilon_3)/2 \qquad (2)$$

$$r = \frac{1}{\sqrt{2}}\sqrt{(\varepsilon_1 - \varepsilon_2)^2 + (\varepsilon_2 - \varepsilon_3)^2} \qquad (3)$$

The graphic representation of the *r(D)* function allows rapid semi-quantitive interpretation of the deformation mechanism [7].

Acoustic ultrasound interrogation set-up

The acoustic measurements are carried out in ultrasound interrogation mode using a pair of lead zirconate titanate ($Pb[Zr_xTi_{(1-x)}]O_3$ –PZT) ceramic, piezoelectric transducers, one operating as an emitter of ultrasound and the second as a receiver. In one first series of experiments, the acoustic coupling has been carried using high-end piezo-electric transducers R15-α (black / narrow bandwidth / emitter) and F15-α (white / wide bandwidth / receiver) manufactured by Euro Physical Acoustics. Same type of experiments have been repeated using low cost sensors from the type EPZ-20MS64W (6.4 kHz, 400 ohms), which possess similar footprint. The acoustic coupling set-up with both type of sensors attached on cells with strain gauges is presented in the supplementary information (S2). The acoustic signals were generated using WaveGen software (company Mistras) allowing defining the characteristics (frequency, duration, amplitude) of the electric signal by an electronic wave generator ARB-140. For the R15-α / F15-α transducers, signal emitted was a frequency sweeping between 100 and 200 kHz, 200 ms long, with a signal amplitude of 0.1 V. For the low cost EPZ-20MS64W transducers, the emitted signal had to be adapted to the and the frequency sweeping was only ranging between 120 and 150 kHz, while the duration was increased up to 1.5 ms and a signal amplitude of 1 V. The electric signal is converted in acoustic wave by the piezoelectric transducer operating in emission mode. The received acoustic signal is the transformed into voltage by the opposite piezoelectric transducer. The received signal is pre-amplified using a PCI2 module (company Mistras). The data acquisition is carried out using AEWin software and analyzed further using Noesis software and in-house developed machine-learning software [8]. The supplementary data (S3) presents the routine of the data analysis starting with the spectral transformation of the detected acoustic waveform and the subsequent clustering and mapping of the power spectra. The in-house developed machine-learning software allows pairing a given State of Charge (SOC) point to a corresponding power spectrum presented as a particular

color in the 2D map.

Results and discussion

Lithium ion cell components

The inspection of the cell casing with SEM and EDX indicated that the iron and nickel are the main constituents of this component. The characterization of the separator material with DSC and FTIR showed the material is composed of polyethylene. Its surface facing the negative electrode is coated with alumina. The separator thickness is about 8 µm. The results from the chromatographic analysis of the electrolyte showed that the solvent is comprised of ethylene carbonate, dimethyl carbonate and propylene carbonate in approximate molar ratio of 6:3:1, being in good agreement with the literature [9]. The analysis of the positive electrode material with XRD, SEM and EDX showed that its principal constituent is $Li_xNi_{0.83}Mn_{0.07}Co_{0.1}O_2$ composition. It is fairly close to the commercial materials from the type NMC 811 having a specific capacity of about 200 $mAh.g^{-1}$ [10]. The measured surface loading is equal to 20.2 $mg.cm^{-2}$, resulting in an approximate specific capacity of 4.04 $mAh.cm^{-2}$. The same type of analysis applied on the negative electrode showed that it is comprised of graphite containing minor silicon content (detected as SiO_2). The surface loading of the negative electrode is 11.9 $mg.cm^{-2}$. The theoretical capacity of the negative active material is about 335 $mAh.g^{-1}$, considering a utilization of the graphite equal to 95 % (C_6 conversion to LiC_6) and the use of 5 % of conductive and binder additives. Thus, the specific capacity of the negative electrode should be about 3.99 $mAh.cm^{-2}$. This value is close enough to those of the positive electrode, allowing the assumption that both electrodes are "balanced" electrochemically.

Mechanic behavior of the cell during charge/discharge cycling

Figure 1 presents the evolution of the ensemble of battery parameters monitored during a short-term galvanostatic cycling with 2h-rated current at 25°C maintained in a climate chamber. During cycling, the cell skin temperature varies between 26 and 31°C, because the MJ1 technology corresponds to the so-called "energy" type and the applied current is close to the tolerance limits. The parameter SOC is calculated posteriori using amp-hour counting. Prior to this cycling, the cell has been completely recharged using constant current / constant voltage sequence (CC / CV, 1.7 A / 4.2 V) terminated when the current during the CV stage decreases to 0.17 A. After 30 min long rest period the strain signals measurement equipment has been reset. Thus, the reference point corresponding to zero deformation has been set to SOC = 100%. The data plotted in Figure 1c show that the strain evolution of all three gauges follows repeatable cyclic pattern that correlates well with the state of charge of the cell, being in good agreement with the literature [5, 11, 12].

The amplitude of the signal from the gauges J1 and J3 is roughly twice of the amplitude of the central gauge J2. This is an indication that the main type of cell deformation is due to the jellyroll diameter shrinkage during the discharge and expansion during the charge. It can be explained well with the fact that the graphite constituting the negative electrode material occupies largest volume fraction of the cell and it experiences most significant crystal lattice expansion due to the lithium ions intercalation (about 17%, [5]).

A closer inspection of the strain signal pattern shows that the relationship between the deformation and SOC is not perfectly straightforward. From one hand, there are small excursions of the strain in the initial and final stages of the discharge (*i.e.* the discharge starts and ends with short expansion periods). From the other, there is significant mechanical relaxation during the rest periods following the termination of the charge process. A hypothesis suggesting that the relaxation is linked with the temperature cool down could be

rejected taking into account the fact that the heating is more intense in the end of the discharge where the amplitude of the relaxation is much smaller.

Figure 1d presents the evolution of the received acoustic signal strength during the constant current cycling measured by the couple piezo-electric transducers R15-α / F15-α. The selected parameter (the integrated voltage signal of entire waveform) allows a first order assessment of the mechanism of interaction of the cell with the probing ultrasound waves. It can be seen that the ultrasound interrogation results correlate with SOC in a way similar to the case of the strain evolution. This correlation suggests that the jellyroll shrinkage enhances some dampening effect or an increased absorption of the ultrasound waves and vice versa (the charging increases the jellyroll compacting which may enhance the passage of the ultrasound).

The results presented in Figure 2 illustrate the impact of the cycling current on the mechanic behavior of the cell. It can be seen that the evolution of the strain and the strength of the received acoustic signal follow similar pattern and amplitude, despite the increased cell temperature during the last cycle with 2 h rated current. The latter supports the above hypothesis that the impact of the Joule heat on the mechanic behavior of the cell during the 2 h – rated cycling is relatively small. The decrease of the cycling current leads to the appearance of much better pronounced regions (local minimums and maximums, changes of the slope) in the strain transients, which should correspond to the lithium ion insertion and extraction inside the different crystallographic phases, formed in the electrodes during the charge/discharge operation. The most significant impact of the current can be seen in the end of the charge process and the subsequent rest period. While the strain maximum reached at the moment of the current cut-off (4.2 V) remains rather constant, the subsequent relaxation process depends on the cycling rate. It can be related to the fact that the lower charge current injects higher number of Amp-hours corresponding to slightly larger jellyroll diameter at steady state.

The strain data shown in Figure 2c have been subjected to the parametric analysis described (Equations 2 and 3). The corresponding results are plotted in Figure 3 together with a guiding diagram for qualitative interpretation of the deformation mechanism [7]. The data points corresponding to the rest periods between the charge and he discharge stages have been removed for the sake of simplicity. The results show that the deformation mechanism does not depend much on the applied cyclic rate, the only exception being the end of the charge domain. The deformation pattern during most of the charge and discharge duration corresponds to a process combining cylindrical shrinkage and compression, *i.e.* isotropic growth of cylindrical body. The data corresponding to the charge and the discharge processes are clearly separated by an elastic hysteresis loop which is related to the energy dissipation due to the lithium ion insertion and extraction from the host matrix of the positive and the negative electrode materials.

Figure 4a presents the results from the clustering and 2D mapping of the received ultrasound signal obtained during cycling with various charge rates and discharge rate fixed at C/2h at 25 °C. The measurements has been carried out with R15-α/F15-α couple of piezoelectric transducers. The different colors account for different types of waveforms defined from their power density spectra (same color = same DSP). Three waveform samples corresponding for different SOC values close to 0, 50 and 100 % are shown. The coupling of the acoustic and the electrochemical data is shown in Figure 4b and 4c using two type of x-axis in order to take into account the evolution of the data as a function of the time and SOC keeping the same color-code. It can be seen that nature of the transmitted acoustic signal changes with the change of the battery SOC almost independently on the applied charge rate. This result remains quite reproducible and it is consistent with the data presented in Figure 3c. The comparison of the data plotted in Figure 4 with those in Figure 2d shows that the acoustic interrogation is able to provide reliable and accurate data about the battery state without the necessity to development of precise physical mode representing the interaction of the cell jellyroll with the probing ultrasound.

Mechanic behavior of MJ1 Li-ion cell in cyclic voltammetry mode

The cyclic voltammetry with low voltage sweep rate (50 $\mu V.s^{-1}$) allows further assessment of the link between the kinetics of the charge/discharge reactions in the cell and its deformation. Figure 5 presents the evolution of the ensemble of battery parameters monitored during this type of test using another cell from the same purchase batch. The data are separated in two parts – the cathodic branch of the plots corresponds to the results measured during the voltage decrease from 4.2 to 2.5 V. Thus, the cathodic sweep can be considered as an alternative 10h rated discharge (its precise duration is equal to 9 h and 27 min). In the same way, the data recorded during the anodic voltage sweep from 2.5 to 4.2 V represent the kinetics of the charge reactions and the associated mechanic phenomena. The evolution of the three strain gauge signals is presented in Figure 5a. It can be seen that the amplitude of the deformation is lower in comparison with the previous case, however it remains in the same order of magnitude. In the voltage domain 3.5 – 4.2 V the signals of the gauges J1 and J3 are nearly identical and they are twice lower than those of J2. These data indicated that the discharge process in this voltage domain corresponds to a cell shrinkage with relatively homogeneous spatial distribution of the local current density. This means than at high SOC values most of the deformation can be related to the lithium ion insertion and extraction from the graphite negative electrode. When the voltage is lower than 3.5 V, the discharge process continues with partial recovery of the cell volume (swelling), which can be linked with the lithium ion insertion in the host matrix of the positive NMC electrode. Here the difference between the signals of the gauges J1 and J3 indicates certain non-homogeneity of the current density distribution. Such type of artefact can be possibly related to the radial positioning of the strain gauge rosette, which cannot be predicted or controlled without preliminary X-ray tomography (e.g. rosette installed in close proximity to the jellyroll foil edge or coating ending).

The parametric analysis of the strain pattern presented in Figure 5b remains similar to those shown in Figure 3. The data corresponding to the anodic and the cathodic sweep are separated by a hysteresis of nearly 60 ppm in direction of both axis, which is fairly close to the hysteresis observed in Figure 3 (about 50 ppm in both directions). The *r(D)* curve contains 4 kink points indicating drastic changes of the mechanism of the cell deformation. The origin of the points corresponding to cell voltage equal to 2.5 and 4.2 V is clear – it corresponds to the termination of the processes of discharge and charge. Both remaining points correspond to cell voltage values close to 3.5 V, *i.e.* they are located in the region of the transition from shrinkage to expansion and *vice versa*. The slope of the parametric function *r(D)* in both regions is distinctly different indicating different mechanisms of expansion and shrinkage of the positive and the negative electrode. It was already mentioned that at higher SOC values, the negative electrode contributes more to the cell deformation and the latter undergoes isotropic cylindrical expansion and shrinkage.

In contrast, it can be seen that the deep discharge carried out in voltammetry mode reveals that the positive electrode contributes to deformation with spherical pattern.

Both sweeps of the classic voltammogram has been separated in order to compare the current with the strain rate (the time derivative of the strain). Since the strain rate of all three gauges follows identic pattern only the parameter corresponding to the gauge J2 is presented in Figure 5c and 5d. The comparison of the strain rate with the current is very convenient because both parameters are time derivatives of physical terms related to the size of the electrochemical cell (diameter, length and charge storage capacity). The sign of the strain rate indicates the deformation type (shrinkage or expansion), while the appearance of minimums and maximums indicates the occurrence of electrochemical reactions. It can be seen that there is a fair correspondence between the number and the position of the current peaks of the strain rate minimums and maximums.

Impact of the temperature on the mechanic behavior of MJ1 Li-ion cells

The impact of the temperature on the mechanic behavior of the MJ1 cells has been evaluated in two different types of experiments. During the first one, completely charged cell equipped with strain gauge rosette has been subjected to a short thermal cycling between -5 and +45 °C using the stair-case like profile shown in Figure 6a. The same plot presents also the evolution of the signals from the three strain gauges. It can be seen that the mechanical response to the change of the temperature is very rapid. It also includes strain relaxation effects with an amplitude increasing over the temperature. The strain *vs.* temperature plots presented in Figure 6b show that the thermal dependence of the deformation is not linear and it features a hysteresis effect which is more pronounced at the higher temperatures. The distinct difference between the inclined gauges J1 and J3 and the central gauge remains, which indicates that considerable part of the thermal effect on the strain signal is related to the mechanical changes of the cell. If we consider that the thermal dependence of the gauge factors remain close to linear, the parametric analysis of the r(D) function can be applied in order to analyses the deformation mechanism related to the changes of the temperature. The corresponding result presented in Figure 6c differs significantly from the data discussed in the previous paragraphs. It can be seen that temperature changes can be associated with nearly ideal shrinkage and expansion of the cell diameter. The hysteresis effects are also much smaller, which indicates that the hysteresis observed in Figure 3 and 5b are caused by the energy dissipation corresponding to the occurrence of the electrochemical reactions.

Figure 7 presents the results from the clustering and 2D mapping of the received ultrasound signal obtained during cycling with 2h-rated charge and discharge current at three different temperatures (5, 25 and 45 °C). Again, the study has been carried out with R15-α/F15-α couple of sensors. As expected, the increase of the temperature increases the capacity and the energy efficiency of battery, the latter being directly evident as decreased voltage hysteresis. It can be seen that the temperature impacts also strongly the waveform of the received ultrasound signal at a fixed cell voltage (respectively fixed SOC value) indicating that the thermal expansion of the cell influences its interaction with the ultrasound. The increase of SOC increases the difference between the acoustic waveform patterns. A smaller variation of the waveform pattern at very low SOC can be seen in Figure 7d. These results can be further related to the fact that the cell jellyroll is the most compact when SOC is close to 0 %, and the additional shrinkage caused by the cooling will not alter substantially the transfer of the ultrasound waves across the cell.

Impact of the cycling aging on the mechanic behavior of MJ1 Li-ion cells

A MJ1 Li-ion cell equipped with strain gauge rectangular rosette and a pair of low cost piezoelectric transducers from the type EPZ-20MS64W has been subjected to charge/discharge cycling with 2h-rated current and depth of discharge equal to 100 % (DOD = 100 %) at room temperature (22 °C +/- 1 °C). Figure 8a and 8b present the impact of the ageing on the classic battery parameter set (current, voltage, temperature and capacity). As expected, the capacity decreases and the internal resistance increases progressively without any significant change of the cell skin temperature. The strain data presented in Figure 8c-8e show that the cycle ageing takes place without causing any significant change of the overall deformation pattern. The most visible impact of the ageing is an increasing amplitude of the signal corresponding to increased cell swelling in charge mode followed by relaxation. In contrast, the strain measurements at open circuit in completely charged state increase with much slower rate especially until 400 cycles. This result indicates that the stress effects associated with the increased swelling of the cell (corresponding on its turn to the lithium ions intercalation in the graphite) are dynamic. This mechanic phenomenon is quite similar to the increased charge voltage due to the higher internal resistance of the cell.

The parametric analysis of the strain data presented in Figure 8f shows that the predominant deformation pattern remains the isotropic growth and shrinkage of a cylindrical body. However the shift of the curves in right-hand direction indicates that the cell swelling caused by the cycling ageing follows a pattern corresponding to a spherical growth, which has been identified as an effect caused by the operation of the positive electrode. Another minor consequence from the ageing is a small decrease of the hysteresis of the *r(D)* plots. This effect can be explained supposing that that the hysteresis corresponds to a certain energy storage capacity. Thus, the large hysteresis corresponding to the charge/discharge cycling can be related to the large electric energy storage capacity (12.6 Wh) and the much small hysteresis observed during the thermal cycling will be due to the much smaller heat storage capacity (0.68 Wh considering C_p = 1 $J.g^{-1}K^{-1}$ and ΔT = 50 K [13]). Using the same consideration we can link the decreasing capacity with the decreasing hysteresis of the *r(D)* plots.

The results from the ultrasound interrogation at different state of health using an acoustic set-up with low cost piezoelectric transducers are plotted in Figure 8g. It can be seen that in this narrow frequency range of acoustic interrogation (120 – 150 kHz), the signal strength dependence on SOC follows an inversed trend – it decreases during the charge and vice versa. The range of this parameter is about one order of magnitude higher. This kind of differences can be explained by the different characteristics of the low cost transducers (e.g. frequency bandwidth, input impedance, coupling mechanism, etc….). No matter of this, the measurements remain rather stable. The effect of the aging is mostly visible at the plateau regions corresponding to the open circuit periods. In this case, the decrease of the capacity correlates with decrease of the signal strength. Figure 8h indicates that the correlation is close to linear, especially when the cell is completely discharged.

The continuous monitoring of both types of mechanical parameters during long-term cycling shows that the impact of the state of charge remains predominant, while those of the state of health cause a slow, rather monotonic drift of the observed mechanical characterization signals.

Conclusions

Two different types of non-invasive mechanical characterization methods have been used simultaneously for extended battery monitoring during its normal operation. Both type of parameters correlate well with the state of charge and the temperature in a stable and repetitive way. The use of rectangular strain gauge rosette and parametric analysis of the signals allows distinguishing two different deformation mechanisms corresponding to the expansion and shrinkage of each electrode due to the intercalation and extraction of the lithium ions. Both electrode shrinkage/expansion mechanisms differs from the deformation caused by the change of the temperature. The acoustic interrogation data show strong dependence on the state of charge and the temperature, especially when the results are analyzed with data-mining tools based on signal clustering and mapping of the power density spectra. It has been found that the method can be also applied successfully using low cost piezoelectric transducers, which provide accurate and stable data during long term cycling aging tests. The acoustic data during such tests undergo rather slow evolution indicating the robustness of the acoustic interrogation as a method for monitoring of the normal battery operation.

Acknowledgement

This work has been realized in association with INES.2S within the French national program Investments for the Future (ANR-10-IEED-0014-01) and received funding from the European Union's Horizon 2020

research and innovation program under the grant 'Electric Vehicle Enhanced Range, Lifetime And Safety Through INGenious battery management' (Project EVERLASTING-713771).

References

1. T.M. Bandhauer, S. Garimella, and T.F. Fuller, J. Electrochem. Soc., **158**, R1 (2011)
2. H. Liu, Z. Wei, W. He, J. Zhao, Energy Conversion and Management, **150**, 304 (2017)
3. X. Feng, M. Ouyang, X. Liu, L. Lu, Y. Xia, X. He, Energy Storage Materials, **10**, 246 (2018)
4. J. Warner, "The Handbook of Lithium-Ion Battery Pack Design", Elsevier, Amsterdam, 2015, p. 91
5. H. Popp, M. Koller, M. Jahn, A. Bergmann, J. Energy Storage **32**, 101859, (2020)
6. Fred Lambert, electrec website, Feb. 3rd 2021, available online at https://electrek.co/2021/02/03/panasonic-plans-tesla-4680-battery-cell-production/
7. Jean Avril, "Encyclopédie Vishay d'analyse des contraintes encyclopédie", NT 58C "Interpretation des mesures extensometriques", Micromesures, 1984
8. L. Oca, N. Guillet, R. Tessard, U. Iraola, J. Energy Storage, **23**, 29 (2019)
9. J. Sturm, A. Rheinfeld, I. Zilberman, F.B. Spingler, S. Kosch, F. Frieb, A. Jossen, J. Power Sources, **412**, 204 (2019)
10. NEI Corporation, "Lithium Nickel Manganese Cobalt Oxide (NMC811) electrode sheets", product brochure available online at https://www.neicorporation.com/specs/NANOMYTE_BE-56E_NMC811_Spec_Sheet.pdf
11. L. Willenberg, P. Dechent, G. Fuchs, M. Teuber, M. Eckert, M. Graff, N. Kürten, .D.U. Sauer, E. Figgemeier, J. Electrochem. Soc., **167**, 120502 (2020)
12. Liyuan Feng, Shuo Zhou, Yancheng Li, Yao Wang, Qiang Zhao, Chunhui Luo, Guixin Wang, Kangping Yan, J. Energy Storage, **16**, 84 (2018)
13. H. Maleki, S. Al Hallaj, J.R Selman, R.B. Dinwiddie, H. Wang, "Thermal properties of lithium-ion battery and components", J. Electrochem. Soc., **146**, 947 (1999)

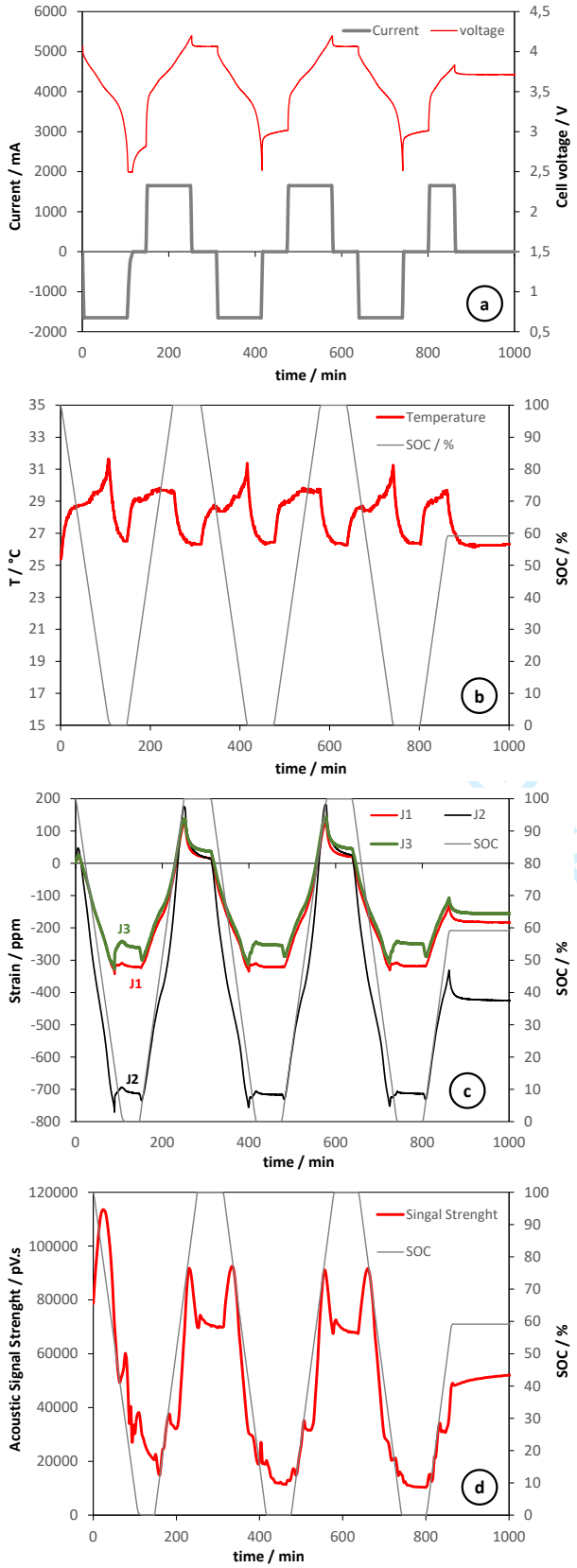

Fig. 1. Evolution of the battery parameters during galvanostatic cycling with C/2h rated current.

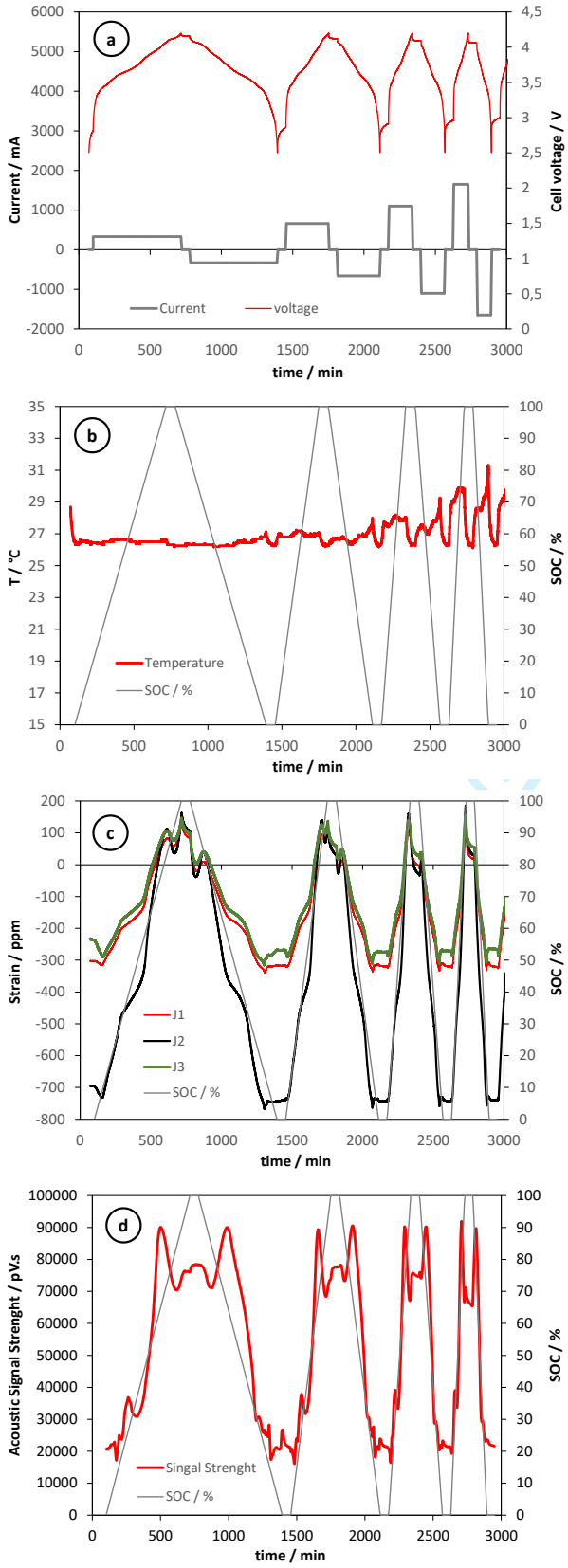

Fig. 2. Evolution of the battery parameters during galvanostatic cycling with current equal to C/10h, C/5h, C/3h and C/2h.

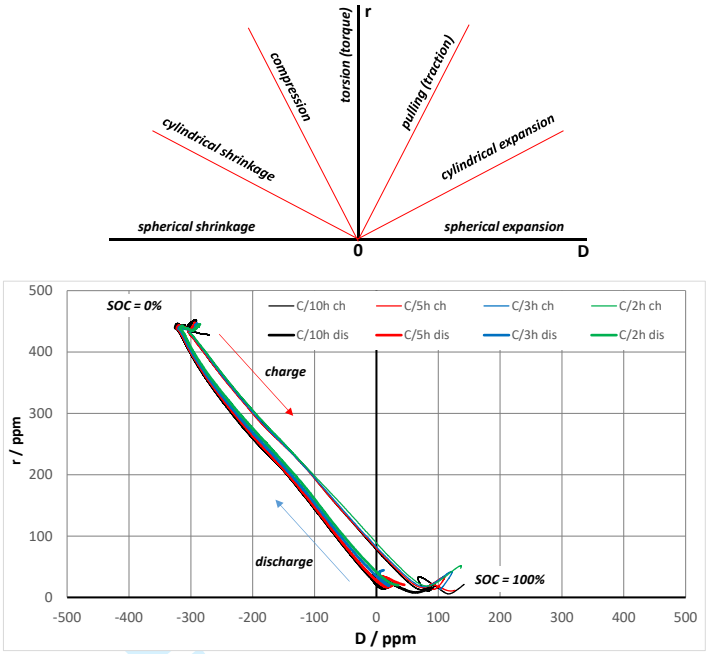

Fig. 3. Parametric analysis diagram for qualitative interpretation of strain measurements carried out by rectangular rosette gage and experimental r(D) patterns obtained during cycling of MJ1 cell with different currents at 25 °C

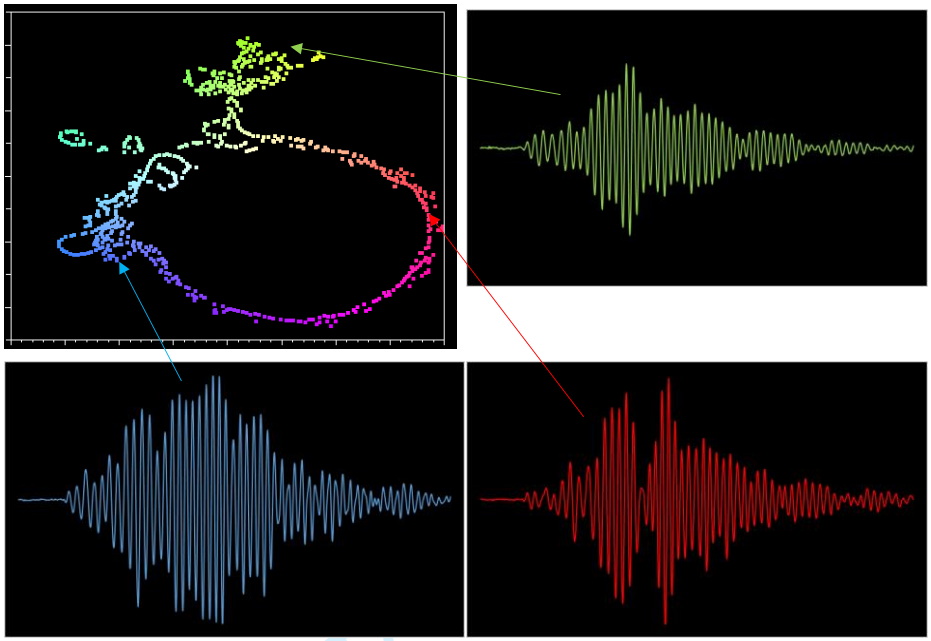

(a)

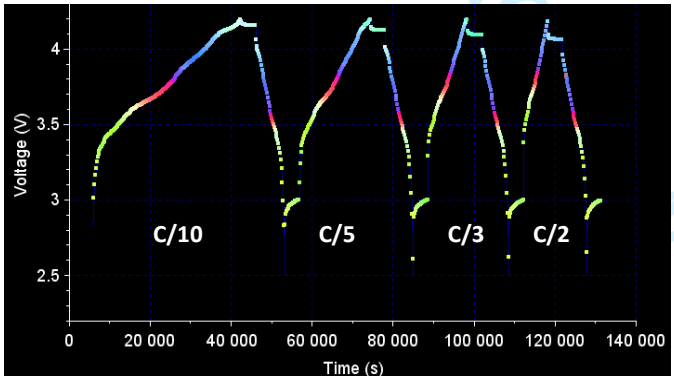

(b)

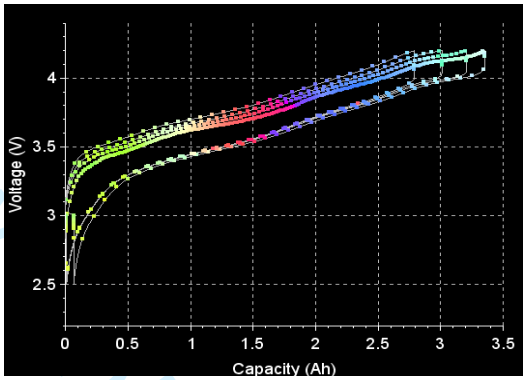

(c)

Fig. 4. Results from the ultrasound interrogation of Li-ion cell INR 18650 MJ1 during cycling with various charge rates and discharge rate fixed at $C_n/2h$ at 25°C (a, b) using clustering and 2D mapping of the acoustic data (c).

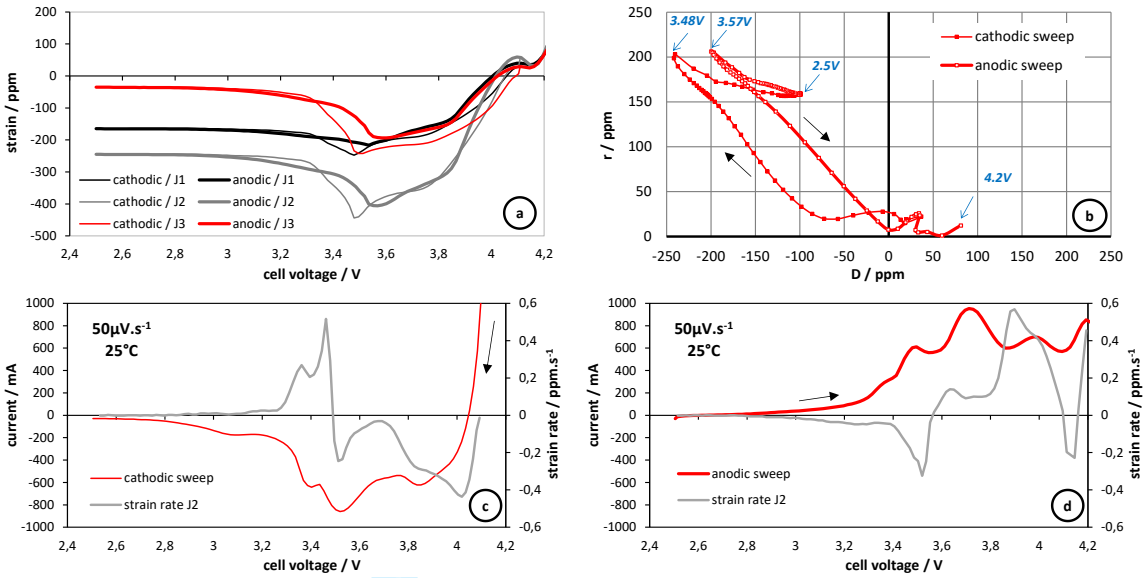

Fig. 5. Evolution of the cell strain (a), current and strain rate (c and d) during voltammetry cycle with sweep rate equal to 50µV.s^{-1} at 25°C, together with the corresponding parametric analysis of the deformation data (b).

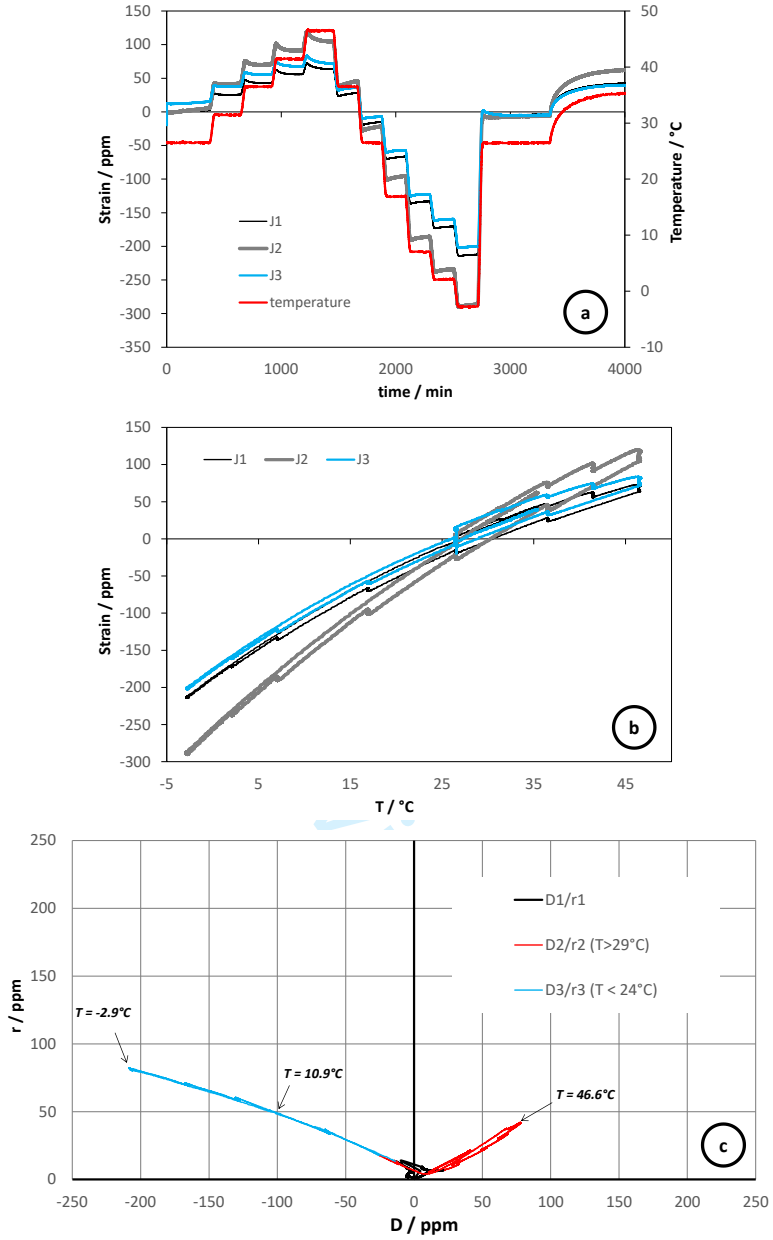

Fig. 6. Impact of the temperature on the strain signal at SOC = 100% (a and b) and parametric analysis of the strain data during the thermal cycling (c). The domains D1/r1, D2/r2 and D3/r3 indicate data points measured corresponding to three different temperature ranges.

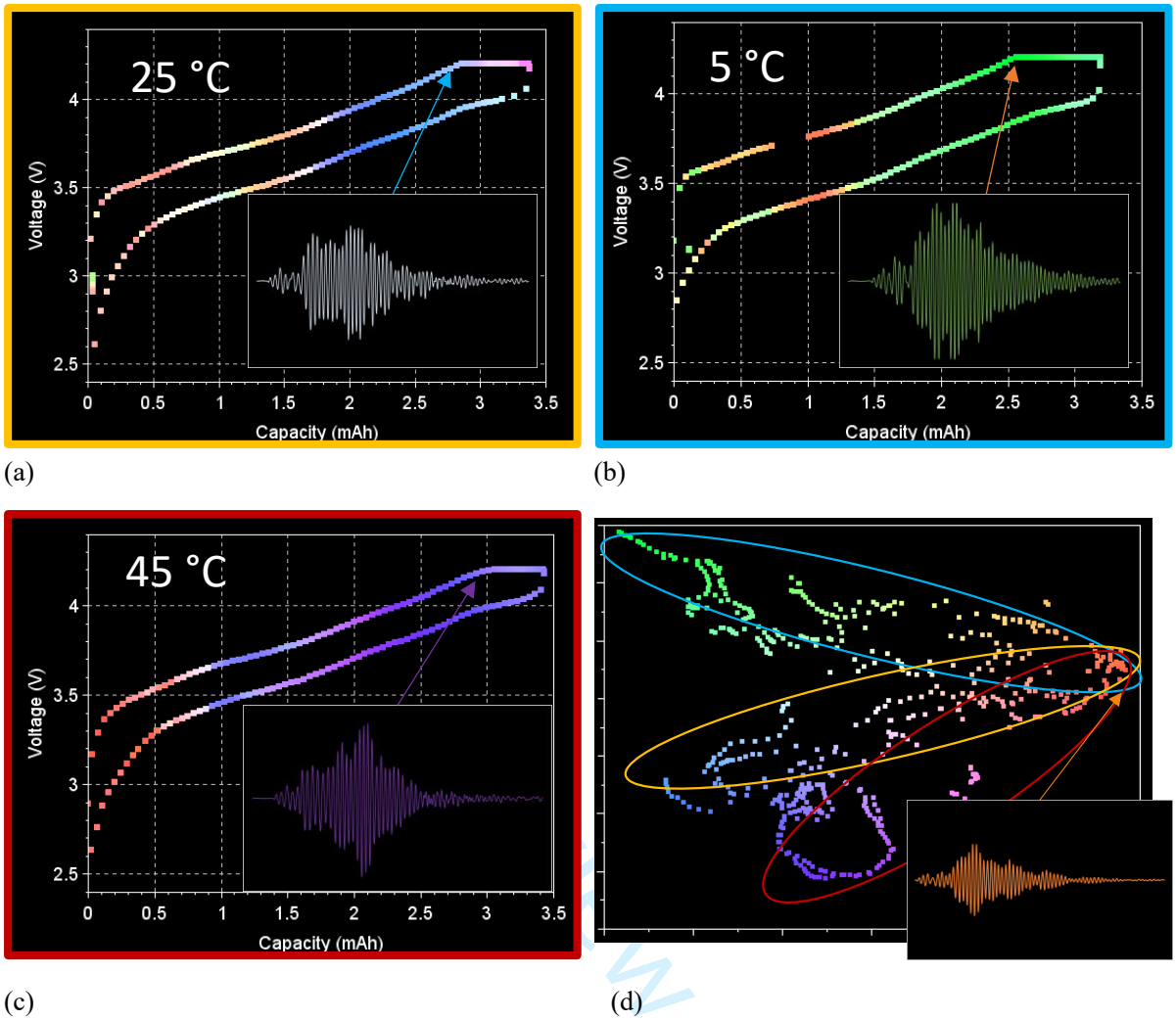

Fig. 7. Results from the ultrasound interrogation of Li-ion cell INR 18650 MJ1 during cycling at three different temperatures with 2h-rated charge and discharge current (a, b and c). Clustering and 2D mapping of the results measured at the different temperatures (d).

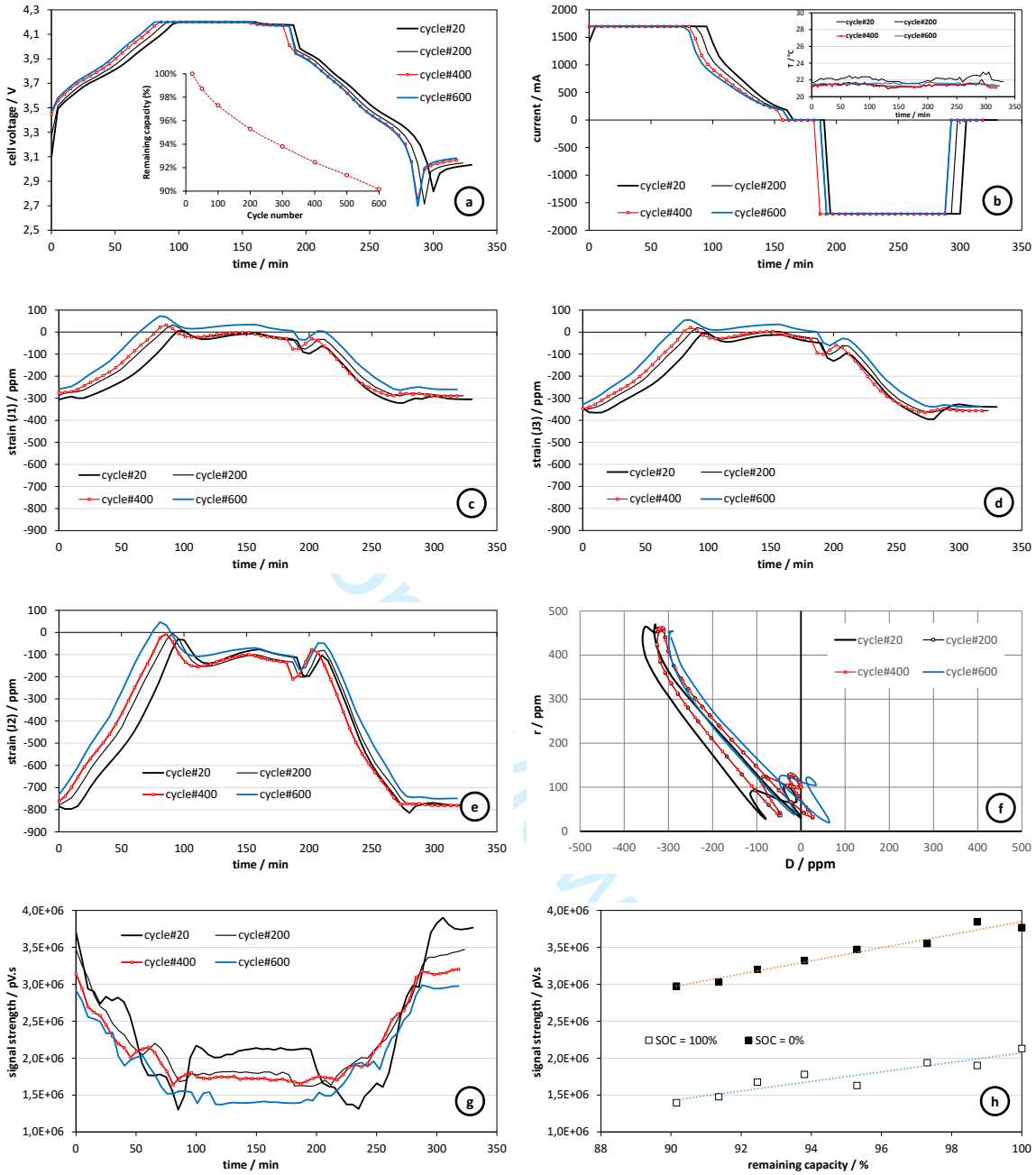

Fig. 8. Impact of the cycling ageing on the electrochemical and mechanical behavior of Li-ion cell INR 18650 MJ1.